Dynamics of Early Neoproterozoic accretion, west-central India: II 1.65 Ga HT-LP and 0.95 Ga LT-HP metamorphism in Godhra-Chhota Udepur, and a tectonic model for Early Neoproterozoic accretion

Anwesa Banerjee, N. Prabhakar, Nicole Sequeira, Nathan Cogné, Abhijit Bhattacharya

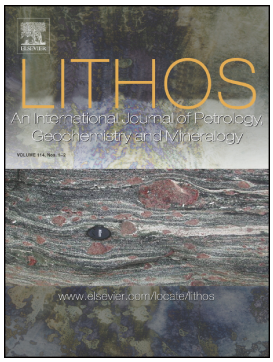

Dynamics of Early Neoproterozoic accretion, west-central India: II ~1.65 Ga HT-LP and ~0.95 Ga LT-HP metamorphism in Godhra-Chhota Udepur, and a tectonic model for Early Neoproterozoic accretion

Anwesa Banerjee, N. Prabhakar, Nicole Sequeira, Nathan Cogné, Abhijit Bhattacharya

PII: S0024-4937(22)00149-9

DOI: https://doi.org/10.1016/j.lithos.2022.106740

Reference: LITHOS 106740

To appear in: *LITHOS*

Received date: 9 December 2021

Revised date: 5 May 2022

Accepted date: 11 May 2022

Please cite this article as: A. Banerjee, N. Prabhakar, N. Sequeira, et al., Dynamics of Early Neoproterozoic accretion, west-central India: II ~1.65 Ga HT-LP and ~0.95 Ga LT-HP metamorphism in Godhra-Chhota Udepur, and a tectonic model for Early Neoproterozoic accretion, *LITHOS* (2022), https://doi.org/10.1016/j.lithos.2022.106740

Dynamics of Early Neoproterozoic accretion, west-central India: II ~1.65 Ga HT-LP and ~0.95 Ga LT-HP metamorphism in Godhra-Chhota Udepur, and a tectonic model for Early Neoproterozoic accretion

Anwesa Banerjee[1*&], Prabhakar N[2], Nicole Sequeira[3], Nathan Cogné[4], Abhijit Bhattacharya[1@]

[1]Department of Geology and Geophysics, Indian Institute of Technology, Kharagpur 721 302, India

[2]Department of Earth Sciences, Indian Institute of Technology Bombay, Powai, Mumbai 400 076, India

[3]School of Earth, Ocean and Atmospheric Sciences, Goa University, Taleigao Plateau, Goa, 403206, India

[4]Plateforme GeOHeLiS, Géosciences Rennes UMR 6118, Université Rennes 1, 35042 Rennes Cedex, France

*Present address: [2]Department of Earth Sciences, Indian Institute of Technology Bombay, Powai, Mumbai 400 076, India

[@]Present address: 180B Hijli Co-operative Society, Kharagpur 721 306, West Bengal 721306, India

[&] Corresponding author.

[&]Corresponding author

Anwesa Banerjee

Email ID: anwesabanerjee21@gmail.com

Phone: +91-9932389411

Email ID of other authors:

Prabhakar N: prabhakarnaraga@gmail.com

Nicole Sequeira: nix.seq@gmail.com

Nathan Cogné: nathan.cogne@univ-rennes1.fr

Abhijit Bhattacharya: abbhat55@gmail.com

ABSTRACT

The N/NNE-striking Aravalli Delhi Fold Belt (ADFB) and the E-striking Central Indian Tectonic Zone (CITZ) converge at the Godhra-Chhota Udepur (GC) sector, west-central India. Analyses of mesoscale deformation structures and metamorphic phase equilibria in the basement and supracrustal rocks are integrated with geochronological-geochemical data (accompanying article) to address the dynamics of the Early Neoproterozoic CITZ-ADFB accretion. In the GC sector, ~1.65 Ga granulite facies anatectic gneisses, ~2.5 Ga and 1.03–1.02 Ga granitoids, and greenschist to amphibolite facies allochthonous supracrustal rocks constitute a tectonic mélange (D2 deformation). The lithodemic units are traversed by networks of W/WNW-striking steep-dipping transpressional shear zones with sinistral kinematics (D3). The shallow-dipping mélange with top-to-the south kinematics is intruded by post-D2 to syn-D3 0.95–0.93 Ga granitoids. Mn-NCKFMASH P-T pseudosection analyses of the anatectic gneisses with pre-D2 garnet + cordierite-bearing leucosomes suggest the rocks evolved along a clockwise P-T path in the range of 5–6 kbar and 680–720 °C. By contrast, the Early Neoproterozoic (0.95–0.93 Ga) chlorite + phengite (Si up to 3.32 apfu) + clinozoisite + quartz ± biotite ± garnet schists in the mélange attained pre/syn-D2 peak metamorphic conditions (10–12 kbar, 450–500 °C). NCKFMASH pseudosection analyses of the ~0.95 Ga phengite-bearing schists indicate the supracrustal rocks evolved along a high-P, low-T clockwise path; phengite-poor micas defining the D3 fabric (Si up to 3.04 apfu) attest to post-peak decompression in the schists. The ~2.5 Ga ADFB granites accreted with the ~1.65 Ga HT-LP anatectic gneisses, 1.03 Ga granites, and the ~0.95 Ga LT-HP supracrustal rocks of the CITZ during D2 thrusting. The crustal convergence continued with the emplacement of post-D2 0.95–0.93 Ga granitoids that culminated with the nucleation of W/WNW-striking D3 transpressional shear zones. This broad contemporaneity among felsic plutonism, LT-HP metamorphism in the supracrustal rocks, and the D2-D3 shortening are

interpreted to be the result of a switch in subduction polarity between 1.03 and 0.93 Ga during oblique ADFB-CITZ convergence.

KEYWORDS: Paleoproterozoic HT-LP anatexis; phengite mica; Early Neoproterozoic LT-HP metamorphism; ADFB-CITZ accretion; subduction polarity reversal; granitoids

1. INTRODUCTION

In accretion settings characterized by clockwise low-temperature, high-pressure metamorphic P-T paths, emplacement of felsic magma generally post-dates collision-related thrust fabrics (Searle et al., 1997; Kuster and Harms, 1998). These granitoids commonly originate due to decompression of the thickened orogen either by tectonic denudation and/or gravitational collapse (Kuster and Harms, 1998). These processes, in turn, are ultimately traced to slab delamination (Meissner and Mooney, 1998), trench retreat (Jolivet and Brun, 2010), lithospheric thinning (Kuster and Harms, 1998) and subduction polarity reversal involving slab breakoff (*Willett and Beaumont, 1994;* Wang et al., 2015).

In the accompanying article (Banerjee et al., 2022a), which develop on the findings of Banerjee et al. (2021, 2022b), the Godhra-Chhota Udepur (GC) sector is demonstrated to be a unique crustal domain where two regional orogenic belts in the Indian Peninsula are juxtaposed, i.e., the E-striking Central Indian Tectonic Zone (CITZ) comprising the Chottanagpur Gneiss Complex (CGC) and the central and southern parts of the Satpura Mobile Belt (SMB) are juxtaposed against the N/NNE-striking Aravalli Delhi Fold Belt (ADFB) (Fig. 1). Such a unique juxtaposition of major orogenic belts (cf. Goscombe et al., 2017) is yet to be documented in Peninsular India. In this sector, Archean (~2.5 Ga) and Late Mesoproterozoic (~1.05 Ga) granitoids, Late Paleoproterozoic (~1.65 Ga) anatectic gneisses (archetypal of the CITZ; Banerjee et al., 2022a, b) and allochthonous ~0.95 Ga supracrustal rocks of

greenschist/amphibolite facies are tectonically juxtaposed into a shallow-dipping tectonic mélange. The mélange was intruded by extensive 0.95–0.93 Ga calc-alkaline S-type granitoids, and some were contemporaneous along a network of basement piercing steep-dipping E-trending transpressional shear zones (accompanying article; Banerjee et al., 2022a). These magmatic and deformational events occurred during oblique NNE-SSW convergence (1.05–0.93 Ga) between the CITZ and the ADFB.

Based on the structural, chronological and geochemical findings in the GC sector located at the western end of the CITZ, Banerjee et al. (2022a, b) demonstrate that the NNE-striking Aravalli-Delhi Fold Belt terminated against the E-striking CITZ at ~1.0 Ga. In this article, we document the metamorphic evolution of the interleaved supracrustal rocks and the Late Paleoproterozoic CITZ gneisses in the tectonic mélange in the GC sector, and integrate the findings of Banerjee et al. (2022a, b) to evolve a geodynamical model for the Neoproterozoic accretion event. This study of Early Neoproterozoic accretion is vital since the CITZ has been correlated with several regional scale accretion orogens across drifted continental blocks (summarised in Banerjee et al., 2021).

2. GEOLOGICAL BACKGROUND

Based on the recent findings (Banerjee et al., 2021, 2022a, b), we highlight the lithological and mesoscale structural aspects of the basement gneisses and the supracrustal rocks relevant to this study. The majority of the basement gneisses are anatectic, especially in the south-central parts of the GC sector. These gneisses with metatexite layers occur as mesoscale enclaves within granitoids; in the absence of regional-scale outcrops, the areal extent of the gneiss exposures cannot be shown in Fig. 1a. The field occurrences of these gneisses in relation to other

lithodemic units are depicted in the 3-dimensional sketch of the overall structural setting in the GC sector (Fig. 1b). These anatectic gneisses are of two mineralogical types. In mesocratic anatectic gneisses, the mineral segregation banding (gneissic layering) is defined by quartz + plagioclase + K-feldspar bearing leucosome layers and biotite + hornblende dominated mesocratic layers that also contain quartz and feldspar in subordinate amounts. Ilmenite, sphene, apatite, monazite and rare zircon are accessory phases, mostly in the mesocratic layers/matrices. These gneisses are non-garnetiferous, in contrast to the melanocratic gneisses in which garnets are ubiquitous and profuse (Fig. 2a, b). In the melanocratic gneisses, the garnet porphyroblasts, rarely larger than 6 mm diameter, occur both within the leucosome layers (Fig. 3a) and in the foliated melanocratic matrix dominated by biotite, quartz, plagioclase, with subordinate amounts of cordierite and sillimanite (Fig. 2b). Garnets are also common within biotite-rich selvages at the leucosome-melanosome interfaces (Fig. 2a).

The leucocratic layers in both types of gneisses exhibit tight to isoclinal folds that exhibit thickened hinges and attenuated limbs; the limbs are commonly boudinaged and exhibit pinch and swell structures (Fig. 3a). In the hinge zone of these isoclinal folds, vestiges of an earlier schistosity, especially well developed in the melanocratic gneisses, mimic the hinges. These folds are intrafolial to the penetrative foliation, which in turn is parallel to the distended limbs of the isoclinal folds. We infer the composite of folded leucosome layers and biotite segregations formed due to D1a deformation, and the later penetrative fabric to be a manifestation of D1b deformation. In zones for high D1b strain, the former D1a schistosity is preserved as mineral inclusion trails in garnet porphyroblasts oblique to the warping D1b fabric (Fig. 2b). Profuse melting (as in metatexite) mark the pre- to syn-D1a deformation stage (Fig. 3a), but syn- to post-D1b melts are lacking or are extremely limited (Banerjee et al., 2022b).

The D1a-D1b composite foliation describes recumbent to gently-inclined D2 folds (Fig. 3b) that plunge W/WNW, broadly parallel to the stretching lineations in the pre-D2 granitoid mylonites (Banerjee et al., 2022b). These folds formed due to top-to-the-south D2 thrusting (Fig. 3c) are superposed by W/WNW-trending open, upright to steeply inclined, and gentle to moderately plunging folds (D3 deformation). These folds are associated with a network of W/WNW-striking steep-dipping transpressional shear zones with sinistral kinematics. The hinges of the D3 folds are collinear with the D3 stretching lineations in the post-D2 and syn-D3 granitoid mylonites (Banerjee et al., 2022b).

The supracrustal rocks are exposed in several parts of the GC sector (Fig.1a, b). The rocks comprise meta-oligomict conglomerate, meta-arenite, micaceous quartzite (quartz, white mica, chlorite), mica schist (white mica, chlorite, quartz, ± clinozoisite/epidote ± biotite ± garnet), metacarbonates (calcite, dolomite, quartz, tremolite, talc, antigorite, clinopyroxene) and Mn-rich horizons, amphibolite (hornblende, actinolite, plagioclase, quartz and clinozoisite). In the ultramafic rocks in the NE of Jobat (Fig. 1a), chlorite, tremolite and Al-poor orthoamphiboles replace embayed grains of relic Mg-rich olivine and pyroxenes (not reported here). The amphibolites are commoner in the northern parts in Fig.1a. The poly-deformed supracrustal rocks were considered to share an unconformable relation with the basement anatectic gneisses and granitoids (Heron, 1934). We observe the basement-cover contact wherever exposed is shallow-dipping and intensely mylonitized; the conglomerate layers in the supracrustal rocks are intra-formational, and no persistent basal conglomerate horizon separates the supracrustal rocks from the underlying basement rocks.

The earliest recognisable fabric in the supracrustal rocks is a colour banding observed in meta-dolomites, marbles and micaceous quartzites. These colour bands, in quarry faces, exhibit

sharp hinged isoclinal folds (D1 deformation). The axial traces of the D1 folds are defined by white mica-chlorite aggregates in mica schists, talc-tremolite antigorite in meta-carbonate rocks and hornblende-plagioclase-clinozoisite/epidote in amphibolites. The D1 schistosity commonly exhibits recumbent to gently-inclined folds and shallow-dipping shear zones (D2 deformation). The D2 folds are round-hinged and isoclinal in metarenites, sharp hinged in metacarbonates and micaceous quartzites (Fig. 3e), and largely obliterated in mica schists. Rootless hinges of the folded D1 schistosity and curved traces of D1 schistosity in D2 microlithons are common in mica schists. The D2 folds are gently-plunging and the axial plane schistosity to D2 folds are spaced and/or zonally developed in the quartzites/meta-rénites and meta-carbonates, but is the most penetrative fabric in the mica schists and amphibolites, except in domains of high D3 strain manifested by W/WNW-striking sinistral shear zones. In these D3 domains, open, upright to steeply-inclined folds with gentle to moderately plunging W/WNW-trending hinge lines in the supracrustal rocks (Fig. 3f, g) the D3 fabrics are transposed to D3 schistosity.

3. PETROGRAPHY AND MINERAL CHEMISTRY

In this section, we present a broad framework of the mineralogy in the allochthonous supracrustal unit and the anatectic basement gneisses. Subsequently, detailed paragenetic relations are presented for selected lithologies and examined in detail for the reconstruction of metamorphic P-T paths. These paths are combined with chronologic and geochemical information in gneisses and granites (accompanying article, Banerjee et al., 2022a) to reconstruct the dynamics of the crustal accretion process. The samples analysed are metacarbonates (AW 70B, AW 157B), mica schists (AW 46B, AW 91, AW 44, AW 82A) and amphibolite (AW 45) in the supracrustal unit, and garnet-cordierite-sillimanite bearing biotite-rich anatectic gneisses

(AW 142A, AW 372) from the basement rocks (Fig. 2). The protocol for determining mineral compositions by Electron Probe Micro Analyzer (EPMA) is in the Appendix A.

3.1 Metacarbonates (AW 157B, AW 70B)

The metacarbonates are dominantly of two mineralogical varieties, e.g., those containing calcite, dolomite, talc, tremolite, chlorite ± kaolinite in the eastern part (represented by AW 70B), and clinopyroxene, plagioclase, calcite, dolomite, quartz and forsterite (pseudomorphed by serpentine) in the western part (represented by AW 157B). The Mn-rich horizons (Das et al., 2009) within the supracrustal unit are excluded.

In the tremolite-talc metacarbonates, the D2 and D3 fabrics are defined by the shape preferred aggregates of talc, tremolite, chlorite and rare kaolinite in a fine-grained recrystallized mosaic of calcite>>dolomite and quartz (Fig. 4a). Tremolite (and talc) also occurs as randomly-oriented post-D3 porphyroblasts (measuring up to couple-of-cms long) and are commonly sieve-textured due to profuse inclusions of quartz, calcite and dolomite (Fig. 4b). In sample AW 70B (Mineral data in Supplementary Material[1]), the MgO contents in dolomite lie between 19.4 and 23.8 wt%; the corresponding values in calcite are < 0.2 wt%. Following the classification of Leake et al. (1997), the clinoamphiboles straddle the boundary between tremolite and actinolite with X_{Fe} [$=Fe^{2+}/(Fe^{2+}+Mg)$] values between 0.06 and 0.10. In the sample, talc and chlorite are Mg-rich [X_{Fe}^{Chl} is in the range 0.08–0.09, and X_{Fe}^{Tlc} lies between 0.04–0.05].

In the calcite-clinopyroxene-plagioclase bearing metacarbonate AW 157B (mineral data in Supplementary Material[1]), the D2 mineral segregation is defined by the alternation of recrystallized aggregates of clinopyroxene-talc-biotite rich (with subordinate amounts of calcite and dolomite) layers and calcite-dolomite-quartz rich layers (Fig. 4c, d). The carbonate-rich

layers are studded with round to elliptical aggregates of randomly-oriented serpentine grains. In rare instances, serpentine also occurs as trans-granular vermiform veins. We suggest these circular mono-mineralic serpentine grain aggregates to be pseudomorphs of former forsterite grains. The ferromagnesian minerals in sample AW 157B are highly Mg-rich, i.e. X_{Fe}^{Bt} [$=Fe^{2+}/(Fe^{2+}+Mg)$] varies in the range 0.05–0.06, and in clinopyroxene, X_{Fe}^{Cpx} varies in the range is 0.04–0.08.

3.2 Mica-chlorite schists (*AW 44, AW 46B, AW 91 and AW 82A*)

The mica schists are dominated by quartz, chlorite and white mica, modally subordinate amount of clinozoisite, and accessory amounts of biotite, sphene and ilmenite. Garnet is a rare mineral observed locally in only one sample. Das et al. (2009) reported kyanite, andalusite and cordierite from several localities. The aluminio-silicate polymorphs and cordierite are lacking in the mica schist samples examined from the supracrustal unit, but cordierite associated with garnet, sillimanite and biotite was observed in the melanocratic gneisses in several localities (see below).

Detailed EPMA data were obtained for four mica schists with somewhat variable mineral assemblages (Tables 1–3), e.g., a garnet-bearing white mica-chlorite-quartz-plagioclase-biotite-ilmenite-magnetite schist (AW 91), a white mica-chlorite-quartz-clinozoisite-plagioclase-biotite-magnetite schist (AW 46B) and a white mica-quartz-chlorite-plagioclase-clinozoisite-sphene-ilmenite schist (AW 44) were selected from the eastern part of the GC sector; and a white mica-chlorite-quartz-plagioclase-clinozoisite-biotite-tourmaline schist (AW 82A) was considered from the western part in the GC sector (Fig. 1a).

AW 44 is a mica schist form D3 low strain domain. The D2 schistosity in the white mica-chlorite-quartz schist is crenulated; the D3 crenulation cleavages are locally developed, and are defined by the same set of minerals (Supplementary Material[3]). Modally subordinate proportion of clinozoisite is restricted to the plagioclase-quartz D2 microlithon. Plagioclase is chemically zoned neighboring the clinozoisite grain aggregates. Sphene occurs as aggregates of discrete grains. In the sample, ilmenite is the only Fe-Ti oxide phase, and occurs as an accessory phase (<1 volume %).

The garnet-free mica schist (AW 46B) occurs as couple of cm-wide layers interleaved with steep-dipping foliated quartzites and meta-arenites in a road cut section. In the outcrop, the mica schist exhibits asymmetric D3 crenulations that are locally transposed to D3 schistosity (Fig. 3g). The crenulated D2 layers are defined by shape-preferred aggregates of white mica-chlorite that alternate with quartz ± plagioclase layers (Fig. 5a). The D3 schistosity is disjunctive, anastomosing and defined by the same set of minerals (Fig. 5a, b). In the D2 quartz microlithons, a pre-D2 tectonic fabric oblique to the warping D2 foliation is also defined by aggregates of chlorite-white mica (Fig. 5b). Clinozoisite occurs in quartz-plagioclase D2 microlithons and as post-D3 porphyroblasts (Fig. 5c). Biotite is an accessory mineral either interleaved with D3 white mica-chlorite aggregates or occurring as discrete post D3 porphyroblasts.

The garnet-bearing mica schist AW 91 exhibits a penetrative steep-dipping spaced, somewhat anastomosing crenulation cleavage (D3) defined by white mica-chlorite layers that alternate with quartz-rich layers containing minor proportion of plagioclase. Garnet occurs in the D3 chlorite-rich domains as small (~200μm diameter) xenoblastic porphyroblasts (Fig. 6a). The rare garnet porphyroblasts appear to overgrow the D2 fabric. but are wrapped by the D3 fabric (Fig. 6a).

The sample AW 82A is a white mica-chlorite-quartz-tourmaline bearing schist with rare post-D2 biotite, and occurs interleaved with an intensely sheared (D2) oligomict quartz pebble conglomerate. Tourmaline and sphene occur as accessory phases in the rock. The penetrative steep-dipping fabric is defined by white mica-chlorite aggregates that alternate with quartz-rich domains. The penetrative D2 fabric defined by the same mineral phases is evident in the D3 intrafolial domains.

The variations in the white mica compositions in the samples AW 44, AW 46B, AW 91 and AW 82A are as follows: Si: 3.14–3.29 apfu; Si: 3.13–3.27 apfu, 3.04–3.27 apfu and 3.06–3.32 apfu, respectively. The corresponding Si/Al values are: 1.18–1.37, 1.20–1.32, 1.13–1.40, and 1.09–1.38; X_{Mg} (= $Mg^{2+}/Mg^{2+}+Fe^{2+}$): 0.48–0.55, 0.46–0.54, 0.23–0.4 and 0.24–0.47; X_{Na} [=Na/(Na+K)]: 0.04–0.06, 0.03–0.06, 0.03–0.17 and 0.03–0.06 (Table 1). Taken together, the corresponding values for the three samples are: Si = 3.04–3.27 apfu; Si/Al = 1.09–1.38; X_{Mg} = 0.23–0.54; and X_{Na} = 0.03–0.17. In each of the samples, several spots in quartz were analyzed to ascertain that the Si abundances in the white micas were not overestimated (Table 1).

The white micas turned out to be phengitic in composition, and in the Na-free system is limited by the compositions of the end member components muscovite [$KAl_{2(}AlSi_3)O_{10}(OH)_2$] and celadonite [$K(Mg,Fe)(Al)(Si)_4O_{10}(OH)_2$] components; the two phase components are related by the exchange vector Al (VI) + Al (IV) → Si^{4+} + (Fe^{2+}, Mg^{2+}) (Cibin et al., 2008). This is the first report of the occurrence of phengite mica from the supracrustal rocks in the GC sector in particular, and the Satpura Mobile Belt and the Chottanagpur Gneiss Complex along the E-striking CITZ (Fig. 1), in general.

The compositions of white mica in the samples AW 44, AW 46B, AW 91 and AW 82A were compared with published compositions of white micas in high-pressure mica schists

elsewhere (Fig. 5d, e). The compositions of our samples overlap with the existing data. In the (Fe^{2+} + Mg) vs Si plot (Fig.5d), the phengite compositions extend from the muscovite end member composition (Fe^{2+} + Mg = 0; Si = 3) towards the celadonite end member (Fe^{2+} + Mg = 1; Si = 4) along the tschermakite substitution vector. Also, in the Al vs Si plot (Fig. 5e), the white micas define a linear trend similar to phengites from other high-pressure rocks collated from elsewhere. The low Ti (0.01–0.03 wt%) and X_{Na} values in the phengites from our samples are also in accord with the samples from around the world, and are indicative of low-temperature, high-pressure (LT-HP) metamorphism (Auzanneau et al., 2010).

However, for any sample, the Si, Al, Fe and Mg contents in the white micas vary considerably (Table 1, Figs. 5d, e). Several authors demonstrably argue that the phengite content in white mica increases with increasing pressure (Krogh and Raheim, 1978; Green and Hellman, 1982; Massone and Schreyer, 1987; among others). In other words, higher abundances of Si, Fe and Mg, and lower Al contents in phengite-richer micas are stable at higher pressure. The variations in our samples could result from chemical zoning in Si, Al, Fe and Mg in individual grains of white mica. Alternately the abundances of the elements could vary depending on the textural setting (multiple deformation fabrics) of white micas in the samples. X-ray element maps for the four elements could not be performed on the finely-interleaved individual grains because the micas were not wide enough for resolving the differences in the element abundances. But wider area high-resolution X-ray maps of Si, Al and Fe (Fig. 5f) were prepared to examine if the white micas defining the different sets of fabrics (i.e., D2 and D3) have different compositions. Several such maps – including maps for K (Fig. 5f) to rule out the presence of quartz and chlorite – exhibit that the white micas defining the D3 fabric are characterized by lower abundances of Si and Fe, and higher abundances of Al relative to those that define the D2

fabric. This indicates that the phengite-poorer micas stabilised at lower pressure define the later D3 fabric.

X-ray elemental maps for Ca, Fe, Mg, and Mn were acquired on one of the two garnet grains in the mica schist AW 91 (Fig 6b, c). Chemical zoning in the garnet ($Alm_{64–71}Prp_{5–10}Grs_{16–17}Sps_{16–11}$; Table 2) is patchy, with no well-defined core and rim regions (Fig. 6b). However, rim to rim compositional gradient exists, e.g. X_{Fe} and X_{Mg} increase towards the D3 chlorite aggregates, with a complementary decrease in X_{Mn} [where $X_i = i/(Fe^{2+} + Mg + Ca + Mn$; where i = Fe^{2+}, Mg, Mn and Ca]; grossular contents vary within 1 mol% (Table 2; Fig. 6c).

Plagioclase in the mica schists is albite in composition, e.g., X_{Ab} [= Na/(Na + Ca + K)] ranges between 0.96 and 0.98 for AW 46B and AW 91, respectively (Table 2). In AW 44, the X_{Ab} varies between 0.85 and 0.90. The Na-rich compositions are obtained in plagioclase mantles neighbouring clinozoisite grain aggregates, whereas the clinozoisite-free parts are more Ca-richer.

The composition of biotite in the mica schists is tightly constrained, e.g. X_{Fe}^{Bt} (= Fe^{2+}/Fe^{2+} + Mg) lies in the range 0.52–0.54 for AW 46B and 0.57–0.59 for AW 91 (Table 2). X_{Fe}^{Chl} (= Fe^{2+}/Mg + Fe^{2+}) in AW 91 varies between 0.57 and 0.61; in AW 46B chlorite is less ferroan and range between 0.48 and 0.52 (Table 2); chlorite in AW 44 is still less ferroan with values ranging from 0.44–0.42. The Mn contents in chlorite for the two samples are 0.03–0.05 apfu and <0.03 apfu respectively. X_{Fe}^{3+} [= $Fe^{3+}/(Fe^{3+}$+Al)] in clinozoisite varies between 0.26 and 0.35 in AW 46B, and 0.16 and 0.18 in AW 91 (Table 2).

3.3 Amphibolite (*AW 45*)

The amphibolite interleaved with mica schists in the supracrustal unit is dominated by Al-rich amphiboles [ferro-tschermakite to ferro-hornblende] and actinolite, and plagioclase (albite) in sub-equal modal amounts; clinozoisite and quartz together constitute upto 15 vol% of the rock, and sphene occurs locally within amphiboles (<3 vol%). Chlorite is a minor mineral (<2 vol%). Nomenclature of amphiboles is after Leake et al. (1997). The rock exhibits two metamorphic fabrics; the penetrative S2 cleavage curves into and is transposed along a spaced S3 cleavage (Fig. 4e, f). Both the D2 and D3 fabrics in amphibolites are defined by the shape-preferred aggregates of co-existing Al-rich and Al-poor clinoamphiboles (Fig. 4e, f). In both fabrics, the amphiboles are intergrown with prismatic crystals of clinozoisite and lentils of plagioclase and quartz ribbons. The clinozoisite grains within the xenoblastic plagioclase grains constitute linear arrays defining the S2 schistosity (Fig. 4f) and exhibit ink-blue interference colour. The clinozoisite grains neighbouring the amphiboles exhibit yellow, first-order red to orange interference colours (Fig. 4f). The colour variation in clinozoisite is a manifestation of their Fe contents; Fe# (calculated as $Fe^{3+}/(Fe^{3+}+Al^{3+})$) for the clinozoisite neighbouring amphiboles are higher and range from 0.12–0.15 while that for the clinozoisite within plagioclase lie between 0.06–0.09. Sphene occurs as discrete grains as well as grain aggregates within the clinoamphiboles.

X_{Fe} [$=Fe^{2+}/(Fe^{2+}+Mg)$] in the Al-rich and the Al-poor amphiboles vary in the range 0.51–0.57 and 0.36–0.38, respectively (Supplementary Material[2]). In the amphiboles, $Fe^{3+}/(Fe^{2+}+Fe^{3+})$ varies in the range 0.01–0.05 and <0.01, respectively (Fe^{3+} in amphiboles computed following Leake et al.'s 1997 formulation). X_{Fe} [$=Fe^{2+}/(Fe^{2+}+Mg)$] in chlorite are intermediate to the amphiboles, e.g. 0.46–0.50. In clinozoisite, $Fe^{3+}/(Al^{3+}+Fe^{3+})$ varies between 0.09 and 0.15. Plagioclase is albite in composition, with An mol% < 4.

3.4 Anatectic basement gneiss (*AW 142A, AW 372*)

The D1a-1b composite layering in biotite-rich gneisses consists of two major parts (Fig. 2a). The melanocratic mosaic in AW 142A (Fig. 2a) and AW 372 (Fig. 2b) is dominated by biotite in a dynamically recrystallized mosaic of quartz and plagioclase, with subordinate amounts of garnet, K-feldspar, cordierite, and sillimanite. The leucocratic part, on the other hand, is dominated by quartz, plagioclase, and modally subordinate amounts of biotite, garnet (Fig. 2a), and rare cordierite (Fig. 2c). K-feldspar is rare in the leucocratic part in Fig. 2a. Garnet and cordierite, (Fig 2c) hosted within leucosomes share stable (non-reactive) boundaries with the associated plagioclase and quartz. Dark selvages of biotite, coarser grained than the melanocratic mosaic, and strongly embayed garnets occur along the margin of the leucosome layers (Fig. 2a). The biotite flakes in the selvages exhibit well developed biotite-defined fabric (D1b) that overprint, and commonly obliterate, the asymmetrically folded former D1a biotite-defined foliation (Fig. 2a). The garnet porphyroblasts in the selvages in AW 142A (Fig. 2a) contain inclusions of biotite, cordierite, plagioclase, quartz and rare sillimanite grains (Fig. 2d). The garnets, in turn, are mantled by double-layered corona, with plagioclase forming the inner collar and aggregates of randomly-oriented biotite grains dominating the outer collar. Randomly oriented chlorite-muscovite intergrowths (Fig. 2e) replace biotite-plagioclase aggregates in the leucosome. Ilmenite, apatite, monazite and rare zircon occur as accessory minerals.

The metamorphic textures in the melanosome are better preserved in the mineralogically homogenous matrix in AW 372 (Fig. 2b), which is mineralogically and chemically similar to AW 142A. The prominent fabric D1b in AW 372 (Fig. 2b) is defined by the aggregates of shape preferred biotite, sillimanite and quartz lentils in a recrystallized mosaic of quartz > plagioclase >

K-feldspar. The D1b fabric wraps around the larger garnet porphyroblasts (Fig. 2b). The larger porphyroblasts, mostly pre-tectonic with respect to the D1b fabric, comprises two parts. The garnet interiors, especially in the coarse grains, exhibit straight to mildly curved trails (D1a) of inclusions of quartz, sillimanite, biotite, and minor proportions of cordierite and feldspars (Fig. 2f). The inclusion trails are oblique and oriented at similar angle to the D1b fabric. The interiors of these garnets are bordered by inclusion-free/poor mantles that, at places, overgrow the D1b fabric. In the smaller garnets, the D1a inclusion trails are either lacking or ill-defined, the porphyroblasts are post-D1b, and sub-idioblastic (Fig. 2g) as opposed to the xenoblastic and skeletal nature of the larger garnets (Fig. 2e). The smaller sub-idioblastic garnets lie almost entirely within biotite aggregates, and appear to overgrow the D1b fabric. As with the coarse garnets, the post-D1a, pre-D1b idioblastic cordierite porphyroblasts also contain inclusion trails of sillimanite and quartz (Fig. 2h). These inclusion trails in the cordierite are oriented sub-parallel to the inclusion trails within the coarse garnet porphyroblasts (Fig. 2b). The coarser garnets are partly or wholly mantled by continuous rims of anhedral cordierite grains (Fig. 2b, f), distinct from the matrix cordierites that occur as idioblastic grains. Strongly embayed grains of garnet, sillimanite and biotite occur as rafts within these post-D1b cordierite grains mantling the garnets. However, the smaller post-D1b garnet grains (Fig. 2g) are not mantled by cordierite.

The biotite-rich melanocratic gneisses, in general, and AW 142A and AW 372 in particular, do not contain sphene and Fe-Ti oxide phases (Fig. 2a, b). However rare grains of pyrite occur as an accessory phase in these gneisses.

Summary of EPMA data of minerals in AW 142A and AW 372 are provided in Supplementary Material[4,5]. Histograms in Supplementary Material[6] show compositional variations in biotite and plagioclase across the melanosome, leucosome layers and the biotite-

rich selvages in AW 142A. In the sample, $X_{Fe}^{Bt, Chl, Crd}$ is defined as $Fe^{2+}/(Fe^{2+} + Mg)$ whereas for garnet X_i is defined as X_i= i/(Fe+Mg+Ca+Mn), where i = Fe^{2+}, Mg, Mn and Ca. X_{Fe}^{Bt} and Ti (apfu) in all biotite grains taken together lie in the range 0.52–0.56 and 0.10–0.17 respectively. No differences in X_{Fe}^{Bt} and Ti^{Bt} (apfu) are evident across the three domains, although biotite in the leucosomes tends to have higher X_{Fe}^{Bt} values. Plagioclase in the three domains is andesine in composition, i.e., 36–42 An mol%; plagioclase compositions in the leucosome are in the range 36–40 mol% An, whereas An contents in melanosome are more sodic, i.e., >38 mol%. The compositions of cordierite and chlorite are tightly constrained, e.g., X_{Fe}^{Crd} across the three domains and X_{Fe}^{Chl} in the melanosome vary in the ranges of 0.36–0.38 and 0.37–0.51 respectively. In AW 372, the Mn content of the ferromagnesian minerals are slightly higher than in AW 142A (Supplementary Material[4,5]); plagioclase in AW 372 is andesine in composition.

The almandine-pyrope garnet porphyroblasts, with subordinate fractions of spessartine and grossular, in both samples are chemically zoned (Fig. 7a–c). The interior of the garnet grains are chemically homogenous, i.e., $Alm_{73–74}Prp_{17}Grs_5Sps_5$ in AW 142A, and $Alm_{71–72}Prp_{16}Grs_4Sps_{8–9}$ in AW 372. Towards the garnet margin, garnet in both samples becomes progressively richer in X_{Fe} and X_{Mn}, poorer in X_{Mg}, and X_{Ca} remains nearly constant (Fig. 7). At the margin, garnet compositions are $Alm_{77}Prp_{10}Grs_4Sps_9$ in AW 142A, and $Alm_{75}Prp_{12}Grs_4Sps_9$ in AW 372 (Fig. 7).

In both the samples, fibrolitic and randomly-oriented rare intergrowths of white mica, chlorite and paragonite (Supplementary Material[4,5]) replace plagioclase, biotite and cordierite (Fig. 2e). The important chemical features in these white micas are the following, e.g. Si = 3.04–3.07 apfu, Ti = <0.02 apfu, X_{Fe} [= $Fe^{2+}/(Fe^{2+} + Mg)$] = 0.44–0.52, X_K [=K/(K+Na)] =0.85–0.90 in AW 142A (based on 14 spot analysis; and Si = 3.02–3.09 apfu, Ti = <0.02 apfu,

X_{Fe} [= $Fe^{2+}/(Fe^{2+} + Mg)$] = 0.44–0.52, X_K [=K/(K+Na)] =0.89–0.94 in AW 372 (based on 8 spot analysis). On the other hand, 4 spot analyses on paragonite yielded, Si = 3.05–3.11 apfu, Ti = <0.01 apfu, X_{Fe} [= $Fe^{2+}/(Fe^{2+} + Mg)$] = 0.45–0.79, X_K [=K/(K+Na)] =0.09–0.16. Clearly, the white micas in the two samples are phengitic, and by implication the high-grade anatectic gneisses experienced the collateral effects of low-T, high-P metamorphism that characterise the supracrustal rocks.

4. METAMORPHIC P-T CONDITIONS

Bakker and Mamtani (2000) and Das et al. (2009) provide information on the metamorphic conditions in the Precambrian rocks from the Southern Aravalli Mountain Belt of which the GC sector is the southernmost part. Based on fluid inclusion studies in quartz and conventional thermo-barometry, Bakker and Mamtani (2000) determined P-T conditions of 2–1.5 kbar and 600–620 °C for metamorphism in the biotite-garnet schists from the Lunavada Supergroup (sample locations unknown). According to Das et al. (2009), the greenschist facies supracrustal rocks of the Champaner Group (in the GC sector) experienced Early Neoproterozoic thermal metamorphism induced by the emplacement of the ~0.95 Ga Godhra granite; however, no quantitative P-T estimates were provided by the authors. In this section, we provide metamorphic P-T conditions (Fig. 8) and metamorphic P-T path reconstructions from the mica schists (AW 46B, 91; Fig. 9) and an amphibolite (AW 45) in the 1.03–0.95 Ga supracrustal unit, and 1.7–1.6 Ga anatectic biotite-sillimanite-garnet-cordierite gneisses (AW 142A, AW 372; Figs. 10, 11). Sample locations are in Fig. 1. Analytical details of the whole rock analysis are presented in Appendix B.

4.1 Mineral thermo-barometry

4.1.1. Supracrustal unit

The P-T estimates for the supracrustal rocks are obtained in white mica-chlorite schists AW 46B and AW 91 (Fig. 8a), and an amphibolite AW 45 (Fig. 8b). For the mica schists, temperatures were estimated using the thermometers garnet-phengite (Krogh and Raheim, 1979; Green and Hellman, 1982), biotite-muscovite (Hoisch, 1989), biotite-muscovite-chlorite (Powell and Evans, 1983) and garnet-biotite (Ferry and Spear, 1978; Perchuk, 1981; Perchuk and Lavrent'eva, 1983; Bhattacharya et al., 1992; Kaneko and Miyano, 2004; Holdaway et al., 1997; Holdaway, 2000; Hodges and Spear, 1982; Indares and Martignole, 1985; Ganguly and Saxena, 1984; Perchuk et al., 1985; William and Grambling, 1990; Hoinkes, 1986). Pressures were estimated from the garnet-muscovite-plagioclase-quartz (GMPQ; Hodson, 1990) and garnet-biotite-muscovite-plagioclase-quartz (GBMPQ; Hodges and Crowley, 1985; Hoisch, 1990) barometers. The garnet-biotite thermometers yield temperatures in the range 420–500 °C; while garnet-phengite thermometers yield somewhat higher temperatures, 470–550 °C (all T values rounded to nearest ten). The biotite-muscovite thermometers yield temperatures in the range 530–650 °C. Pressure estimates obtained from the GBMPQ and GMPQ barometers for phengite-rich muscovite yield high pressures, 10–15 kbar in the temperature range 500–550 °C. The biotite-muscovite-chlorite equilibrium (Powell and Evans, 1983) was applied to both the mica schist samples for the entire range of Si contents in the samples (Si: 3.08–3.27 apfu in AW 46B, and Si: 3.10–3.24 apfu for AW 91) to calculate the lnKd values using the formulations of the authors. The P-T loci for the barometric formulation for the different lnKd values (Fig. 8a) correspond to the whole range of Si contents in the phengites from the samples. Since the compositions of chlorite and plagioclase in each of the samples are similar, the wide variation in pressure at any temperature is a function

of the Si contents of the white micas. Clearly, the highest pressure in each sample is obtained for the micas with the highest celadonite component. In other words, phengite richer D2 micas equilibrated at a high pressure relative to the micas defining the D3 fabrics (Fig. 5f). Based on the results of the thermo-barometric computations, the P-T box (Fig. 8a) deduced from the intersections of the mineral thermo-barometers involving phengite-rich mica assemblages is our preferred estimate of the peak P-T conditions experienced by the mica schists. The preferred P-T conditions (12 ± 1.5 kbar, 500 ± 50 °C) fall in the kyanite stability field (Fig. 8a).

In the amphibolite AW 45, temperatures were obtained using the Al-rich amphibole-plagioclase thermometers of Blundy and Holland (1990) and Holland and Blundy (1994). In the calculations, the cation site allocations for amphiboles were done as per Appendix B of Holland and Blundy (1994). The two thermometers (T_a and T_b) followed by Holland and Blundy (1994) are based on the reactions edenite + 4quartz = tremolite + albite and edenite + albite = richterite + anorthite, respectively. The T_a thermometer of Holland and Blundy (1994) yields higher temperatures (580–720 °C) compared to the T_b thermometric formulation (400–600 °C). The pressure conditions were estimated for AW 45 using the plagioclase-hornblende-quartz barometer of Bhadra and Bhattacharya (2007). The magnesiohornblende compositions yield pressure between 4.4 and 6.0 kbar at 550 °C; by comparison, the ferrohornblende and ferrotschermakite compositions yield larger variations in P values in the range 3.8–7.1 kbar at T = 550 °C. The intersections of the thermo-barometers yield two P-T boxes, e.g., 450 ± 30 °C, 5 ± 2 kbar corresponding to the T_a thermometer and 650 ± 50 °C, 8 ± 2 kbar corresponding to the T_b thermometer.

The difference (~200 °C) in temperature between the T_a and T_b may stem from the fact that the temperatures are calculated from reactions that involve low-Al end member components

such as tremolite and richterite in the high-Al amphiboles. The activities of these end member components in the Al-rich amphiboles are extremely small, and problems relating to site allocation of elements are likely to induce uncertainties in estimating temperature. In any case, the higher set of temperature values in the amphibolites appear erroneous because at these conditions, the metamorphosed arenites and argillaceous rocks within the supracrustal units are expected to experience melting, and white mica and chlorite are unlikely to be stable. These features are lacking in the supracrustal unit. The low-T, high-P metamorphic conditions obtained from the schists (Fig. 8a) are different from the low-P conditions retrieved from the amphibolites (Fig. 8b). The P-T conditions obtained for the amphibolites using the T_a thermometers may correspond with post-peak conditions retrieved from the schists. Also, several researchers suggest that in contractional orogens, metamorphic P-T paths are seldom identical; instead, the P-T paths are diverse because individual crustal domains or tectonic slices within the orogen evolve along distinctive metamorphic P-T paths (Selverstone and Spear, 1985 and references therein).

4.1.2. Anatectic basement gneisses

P-T estimates for the basement gneisses were obtained based on several thermometers and barometers applicable to the garnet-cordierite-plagioclase-sillimanite-biotite-quartz bearing mineral assemblage in samples AW 142A (Fig. 8c) and AW 372 (Fig. 8d). The P-T values in the two rocks were obtained from the two thermometers, e.g., garnet-cordierite (Thompson, 1976; Holdaway and Lee, 1977; Bhattacharya et al., 1988; Perchuk et al., 1985; Wells, 1979) and garnet-biotite (authors mentioned above). Pressures were estimated from the garnet-aluminosilicate-silica-plagioclase (GASP; Newton and Haselton, 1981; Hodges and Spear, 1982;

Ganguly and Saxena, 1984; Hodges and Crowley, 1985; Koziol, 1989; Koziol and Newton, 1988) and garnet-cordierite-sillimanite-quartz (GCSQ; Thompson, 1976; Perchuk et al., 1985; Holdaway and Lee, 1977; Wells and Richardson, 1979; Wells, 1979) barometers. The P-T estimates were obtained using compositions of (a) garnet (core) and biotite (inclusion) and (b) garnet (rim) and nearest neighbour biotite/cordierite in the matrix. For the GASP barometer, the compositions of matrix plagioclase were adopted. The pairs of garnet (core) and biotite (inclusion) yielded higher temperatures (>670 °C), whereas the garnet (rim) and matrix biotite/cordierite nearest-neighbour pairs (not in grain contact) furnished lower temperatures, typically <670 °C. The pressure estimates obtained from each of the two barometers did not vary outside the errors associated with the barometric formulations, i.e., ± 1 kbar. The maximum P-T conditions obtained from the intersections of the thermo-barometers ranged between 4.5–6.2 kbar, 625–725 °C (mean value 5.4 ± 0.8 kbar, 675 ± 50 °C) for AW 142A, and 4.0–6.5 kbar, 600–750 °C (mean value 5.2 ± 1.2 kbar, 675 ± 80 °C) for AW 372. The HT-LP conditions obtained for the 1.7–1.6 Ga pre-D2 high-grade metamorphism in the anatectic gneisses are compared with the 1.03–0.93 Ga D2-D3 metamorphism in the mica schists and amphibolites (for T_a values) in the supracrustal unit in Fig. 8e.

4.2. P-T path reconstruction

P-T paths are reconstructed for the mica schist sample AW 44 (Fig. 9) and two anatectic gneisses, AW 142A and AW 372 (Fig. 10, 11). The bulk rock compositions were obtained by splintering, repeated coning and quartering and pulverising 4–5 kg of the rocks. For reconstructing the P-T paths, the three samples are selected because the rocks do not contain multi-component solid solution (such as hornblende) to avoid problems in reconstructing

topologies of phase fields arising from uncertainties in complex a-X relationships. Also we selected the mineral assemblages in which Fe-Ti oxide phases either occur in accessory amount <1 vol% of whole rock (as in the mica-chlorite schist AW 44; Supplementary Material[3]) or are lacking as in the anatectic gneisses AW 142A and AW 372 (Fig. 2a, b). In addition, ilmenite in the sample AW 44 is a solid solution between ilmenite ($FeTiO_3$) and pyrophanite ($MnTiO_3$) in the molar ratio 0.92 and 0.08 respectively (Table 3), and with negligible amounts of geikielite ($MgTiO_3$) and haematite (Fe_2O_3). The sample (AW 44) with low abundance of Fe- Ti oxide with low Fe_2O_3 content is to ensure the f(O2) conditions need not be retrieved for P-T path reconstruction. This is especially crucial for AW 44 because the mineral assemblage does not permit robust thermo-barometric formulations to be applied, and therefore $f(O_2)$ cannot be determined in the absence of P-T estimates. In the other mica schist samples, either magnetite and/or ilmenite are present in somewhat higher proportion, and ilmenite contains higher mole fractions of Fe_2O_3 in solid solution with ilmenite.

The P-T pseudosections were constructed using the Perple_X software of Connolly (2005; http://www.perplex.ethz.ch/) version 6.9.0 along with the database hp62ver.dat and solution_model_690.dat files. A uniform set of a-X relations was used for the solid solution minerals for the samples. However, for white mica, two different solution models were used to account for the diverse compositions of white mica in the mica schist (AW 44) and the anatectic gneisses (AW 142A, 372). The P-T paths were obtained for the bulk rock compositions based on the phase topology relations, and by comparing, as closely as possible, the theoretical and the measured compositions of minerals, and direction of change in the volume% of critical minerals.

4.2.1. Mica schist (AW 44)

In constructing the NCKFMASHTi P-T pseudosection, the following minerals (in parenthesis) and independent phase components [in square brackets] were adopted: Garnet (Gt) [alm, py, grs, sps], phengite (Pheng) [pa, cel, fcel, mu], chlorite (Chl) [mnchl, daph, ames, afchl, clin], biotite (Bio) [fbi, tbi1, ann, phl, east], plagioclase (Pl) [abh, an], K-feldspar (Kfs) [San], staurolite (St) [mst, fst, mnst], talc (T) [ta, fta, tats], orthopyroxene (Opx) [mgts, en, mots, feots, fs], chloritoid (Ctd) [mnctd, fctd, mctd], carpholite (Carp) [mcar, fcar]. SiO_2 and pure H_2O were taken to be in excess. The solution models used are those of Holland and Powell (2001) for garnet, phengite, chlorite, staurolite, orthopyroxene and chloritoid. The solution models for K-feldspar and plagioclase are adopted from Waldbaum and Thompson (1968) and Newton et al. (1981), respectively. In the computation, the model proposed by White et al. (2007) for biotite was considered. For talc and carpholite, the a-X models listed in the solution_model_690.dat files were adopted.

The bulk rock composition for which the NCKFMASHTi pseudosection (Fig. 9a) was constructed in the P-T window, 2–20 kbar and 450–650°C is composed of (in wt%) SiO_2 = 57.81, TiO_2 = 0.83, Al_2O_3= 19.24, FeO = 6.95, MnO = 0.10, MgO = 3.96, CaO = 0.50, K_2O = 4.75, Na_2O = 0.75, H_2O (loss on ignition, LOI) = 5.40 (Total = 99.79 wt%). The quoted LOI value is computed after drying out absorbed H_2O. The representative ranges of compositions of minerals in AW 44 (Table 3) are the following: D2 muscovite [Si = 3.24–3.26 apfu], D3 muscovite [Si = 3.14–3.19 apfu]; muscovite [Fe = 0.11–0.15 apfu], chlorite [Mg/(Mg + Fe) = 0.42–0.44]; plagioclase [Ab = 0.85 mol%]; clinozoisite (Al/3 = 0.90], and ilmenite [ilmenite: pyrophanite = 0.92:0.08] (Table 3). For the mineral assemblage in AW 44, the P-T window was narrowed down to 5–15 kbar, 410–550°C (Fig. 9b). This P-T window (Fig. 11b) is contoured for Si (apfu) in phengite, the Ab content in plagioclase and X_{Mg}^{Chl} (=Mg/Mg+Fe). At the D1-D2

peak-P, T conditions (Fig. 9b), the relevant phase field comprising white mica, chlorite, clinozoisite, sphene, plagioclase and rutile is limited at higher pressure by lawsonite, glaucophane and chloritoid bearing assemblage, and garnet bearing assemblages occur at the high-T side. In the mica schists, lawsonite, glaucophane and chloritoid are lacking, and garnet is rare. At the peak P-T conditions of 10–12 kbar and 450-550 °C, consistent with the peak P-T estimates (Fig. 8), the computed chemical compositions of the minerals are: Si in phengite [3.24 apfu to 3.20 apfu], X_{Mg}^{Chl} [0.48–0.52], and X_{Ab} in plagioclase lies in the range 0.84–0.80. The pseudosection reconstruction (Fig.11b) shows rutile to be stable in the relevant phase field; the theoretically determined volume % of rutile is ≤ 0.08 for the peak assemblage. Also, rutile is lacking in any of the mica schists, and the stable Ti-bearing phase in AW 44 is ilmenite, present in < 1 vol% of the rock (Supplementary Material 3). A P-T pseudosection was also constructed for the same bulk composition (Fig. 9c) in the NCKFMASH system. The phase topologies and the isopleths change marginally with respect to those in the Ti-bearing system (Fig. 9b). Apparently the inclusion of TiO_2 as a system component effectively stabilised low vol% of rutile and/or ilmenite, resulting in insignificant changes in the phase topologies and the compositional isopleths. The minor disparities between the theoretical and the measured compositional parameters possibly stem from the small errors in the bulk rock estimation and/or the standard state thermodynamic data as well as a-X relations in the multi-component solid solution phases adopted in the computations. We also extended the NCKFMASHTi system to include Mn. But as garnet stability expands due to the preferential partitioning Mn relative to the associated minerals (White et al., 2014), garnet appears as a stable phase in almost all phase assemblages in the P-T of interest for AW 44. This is inconsistent with the rarity of garnet in the mica schists, and hence the Mn-NCKFMASHTi system is not considered.

The retrograde path in AW 44 is difficult to constrain due to the lack of adequate post-D2 mineral assemblages. However the Si-poorer D3 phengite (Table 3; Fig. 5g) interleaved with chlorite and clinozoisite are stable at lower pressure (Fig. 9b), and clearly such assemblages are indicative of decompression following the attainment of the peak-P conditions. The overall P-T path is deemed to be clockwise with decompression ± cooling in the retrograde sector (Fig. 9b). A decompression ± cooling path in the retrograde sector of the clockwise P-T path (Fig. 9b) also explains the sporadic occurrence of post-D3 biotite in the mica schists (Tables 1, 2), although biotite is lacking in AW 44. However, a counter-clockwise P-T path is inconsistent with the structural setting of the supracrustal unit, and also the path does not explain the absence of biotite interleaved with chlorite, phengite-rich mica, chlorite and quartz in the D1-D2 fabrics in any of the mica schists examined, including AW44. This is because biotite in equilibrium with chlorite and lower-Si mica is stable at lower pressure relative to the higher-P biotite-free celadonite richer mica bearing assemblages (Fig. 9b).

4.2.2. Basement anatectic gneisses (AW 142A, AW 372)

Since the gneisses are mineralogically heterogeneous with leucocratic layers comprising 35–40 vol% of the bulk rock (Fig. 3b, d), care was taken to splinter the rock into large blocks so that the leucosome:melanosome proportion was maintained as closely as possible. About 4 kg of the samples were used for obtaining bulk rock compositions. The details in methodology for determining the chemical compositions of the rock powders are provided in the Appendix. The major element compositions (in wt %) for the rocks are as follows: AW 142A [SiO_2 = 61.64, TiO_2 = 0.75, Al_2O_3= 16.20, FeO = 9.90, MnO= 0,03, MgO = 3.96, CaO = 0.95, K_2O = 4.16, Na_2O = 0.82, H_2O (LOI) = 2.30 (Total = 100.71 wt%)]; and AW 372 [SiO_2 = 61.52 TiO_2 = 0.60,

Al_2O_3= 16.52, FeO 10.00, MnO= 0,39, MgO = 2.69, CaO = 2.33, K_2O = 3.10, Na_2O = 1.72, H_2O (loss on ignition, LOI) = 1.73 (Total = 100.60 wt%)]. For the P-T pseudosection reconstructions, the compositions of AW 142A (Fig. 2a, 3b, d) and AW 372 (Fig. 2b) were approximated to the Mn-NCKFMASHTi and Mn-NCKFMASH systems. In the reconstruction of the pseudosections, the following minerals (in parenthesis) and independent phase components [in square brackets] were considered: Garnet (Gt) [alm, py, grs, sps], cordierite (Crd) [crd, fcrd, mncrd, hcrd], orthopyroxene (Opx) [mgts, mots, en, fs, feots], clinopyroxene (Cpx) [esn, ccrts, cats, jd, can, hed, di], olivine (O) [fo, fa, teph, fran], plagioclase (Pl) [abh, an], K-feldspar (Kfs) [San], biotite (Bio) [ann, phl, east, tbi1, fbi], muscovite (Mica) [mu, pa, ma_dqf, cel, fcel, fmu], staurolite (St) [mst, fst, mnst] and melt (Melt) [fo8L, fa8L, zr8L, abL, sil8L, anL, kspL, wi8L, q8L, h2oL]. Quartz is taken to be in excess. The solution models used are those of Holland and Powell (2001) for garnet, staurolite, orthopyroxene, clinopyroxene, olivine and melt, White et al. (2014) for cordierite, White et al. (2007) for biotite, Waldbaum and Thompson (1968) for K-feldspar, Newton et al. (1981) for plagioclase, Coggon and Holland (2002) and Auzanneau et al. (2010) for muscovite.

In the P-T pseudosection reconstructions, the fluid was assumed to be pure H_2O, and the amount of H_2O was constrained by the LOI values in the two gneisses. The LOI value primarily corresponds to the amount of H_2O structurally held in the hydrous minerals (biotite) in the gneisses. The LOI values are expected to be lower than the amount of H_2O initially present in the rocks (pre to syn-D1a) for two reasons. First, the leucosomes occur as continuous layers, and this demonstrates that undefined amounts of melt were able to segregate, and migrate along interconnected D1a porosity networks (Holness, 2018). It is possible therefore that a fraction of the melt may have escaped during and prior to the D1a deformation. Also, melt escape would

render the chemical composition of the rock more restitic relative to the protolith. Second, H_2O is strongly partitioned into the melt phase during melting, and therefore the H_2O dissolved in the melt is likely to have escaped as well. Thus the P-T pseudosection reconstructed using the analyzed bulk rock composition, and the LOI value, are likely to reflect the effects of post-D1a sub-solidus metamorphic modifications experienced by the melt-extracted restitic gneisses. It follows that the supra-solidus pre/syn-D1a P-T history can be qualitatively proposed.

The Mn-NCKFMASHTi and the Mn-NCKFMASH P-T pseudosections for AW 142A (Fig. 10a, b) and AW 372 (Fig. 11a, b) are shown in the P-T window (4.6–7 kbar, 660–820°C) for the mineral assemblages of interest involving quartz, biotite, plagioclase, garnet, cordierite, sillimanite, alkali feldspar and melt (Figs. 10a, b, 11a, b). The phase topologies for the Mn-NCKFMASHTi and the Mn-NCKFMASH P-T pseudosections for each of the two rocks are similar, except that ilmenite appears in less than 1 vol% in the Ti-bearing system for AW 142 and AW 372, both of which lack Fe-Ti oxide phases. Therefore we have retrieved the possible P-T paths from the compositional contours for X_{Fe}, X_{Mn} and X_{Ca} in garnet (Fig. 7), the compositions of biotite, cordierite, plagioclase (Supplementary Material[4-5]) and relative changes in the volume, rather than the absolute modal values, of the minerals (garnet, cordierite and melt) based on reaction textures. These textures relate to (a) the growth of garnet due to incongruent melting reactions at the expense of biotite, sillimanite, cordierite and feldspar, and (b) the increase in the vol% of cordierite via sub-solidus reactions that consume biotite, garnet and sillimanite (Fig. 2a, b).

The garnet core composition in our samples (Fig. 7a) matches well with the theoretical isopleths of X_{Fe}^{Grt}, X_{Mn}^{Grt}, X_{Ca}^{Grt} and X_{Mg}^{Grt} values (Fig. 10a) obtained from the Mn-NCKFMASH P-T pseudosection (Fig. 10b); however the rim compositions of garnets (X_{Fe}^{Grt}

:0.77, X_{Mg}^{Grt} :10 for AW 142A and X_{Fe}^{Grt} :0.75, X_{Mg}^{Grt} :12 for AW 372) in our samples deviate from the X_{Fe}^{Grt} and X_{Mg}^{Grt} compositional contours within the P-T window (Figs. 10b, 11b). The qualitative prograde segment of the P-T path has been inferred to extend from a garnet-free field leading up to the core composition of the garnet ($Alm_{73–74}Prp_{17}Grs_5Sps_5$) in sample AW 142. For AW 372, since there is no Grt free field, the prograde segment has been constructed in the direction of increasing modal abundance of Grt and melt and decreasing modal abundance of Crd leading up to the core Grt composition of $Alm_{71–72}Prp_{16}Grs_4Sps_{8–9}$. This is done to account for the pre- to syn-D1a anatexis that produced garnet at the expense of biotite-sillimanite-cordierite inclusions hosted in the garnets (Fig. 2a, b).

The retrograde segment of the P-T path for both AW 142 and AW 372 has been constructed starting from the garnet core composition ($Alm_{73–74}Prp_{17}Grs_5Sps_5$ in AW 142, and $Alm_{71–72}Prp_{16}Grs_4Sps_{8–9}$ in AW 372) in the overall direction of increase in the X_{Fe}^{Grt} and X_{Mn}^{Grt} contents, increase in the modal abundance of Crd and decrease in modal abundance of Grt. This path accounts for the decrease in volume of garnet due to post-D1b decomposition to double layered biotite-plagioclase aggregates (in AW 142), and the stabilisation of cordierite mantles around garnet via the model KFMASH reaction, $2Fe_3Al_2Si_3O_{12}$ (in Grt) + $4Al_2SiO_5$ (Sill) + $5SiO_2$ (Qtz) → $3Fe_2Al_4Si_5O_{18}$ (in Crd) in AW 372. The P-T path so obtained describes a U-shaped clockwise pattern in both samples (Fig. 10b, 11b). The reconstructed clockwise P-T path, with the peak P-T anatectic conditions during D1a at 5 kbar, 720 °C is followed by a retrograde sector involving decompression (Fig. 10b, 11b). The clockwise geometry in the anatectic gneisses is similar to the P-T paths retrieved in the basement gneisses in the Chottanagpur Gneiss Complex and the southern and central domains of Satpura Mobile Belt (summarised in Banerjee et al., 2021) eastwards within the CITZ vis-à-vis the southern arm of the GIPFOB (Fig. 1).

5. DISCUSSION

5.1 Time of accretion

The significant findings in this study have been the documentation of LT-HP metamorphic conditions along a clockwise P-T path in the supracrustal rocks using multiple mineral thermo-barometric formulations and NCKFMASH P-T pseudosection analyses in quartz-chlorite-white-mica-biotite-albite-clinozoisite ± garnet assemblages. The clockwise LT-HP metamorphism retrieved from AW 44 (Fig. 9) is unique because the metamorphic path is synkinematic with top-to-the-south D_2 thrusting associated with convergence between two regional orogens, e.g. the N/NNE-striking Aravalli-Delhi Fold Belt (ADFB) in the north that terminates against the western end of the E-W striking Central Indian Tectonic Zone (CITZ). The timing of the P-T path in the GC sector may be constrained within reasonable limits. The supracrustal rocks affected by the top-to-the-south thrusting and LT-HP metamorphism was intruded by the 0.95–0.93 Ga blastoporphyritic syn-D_2 granitoids (Banerjee et el., 2022a, b) and post-dated the emplacement of the ~1.03 Ga granitoids (Banerjee et el., 2021a). In addition, the dates retrieved from the idioblastic metamorphic monazites in a mica schist (Banerjee et al., 2022a) range between 1.05–0.92 Ga (Banerjee et al., 2022a). We argue, therefore, that the syn-thrusting clockwise LT-HP metamorphism in the supracrustal rocks (Fig. 9b) occurred in the Early Neoproterozoic, 1.03–0.95 Ga U-Pb dates (Banerjee et al., 2022a, accompanying article).

5.2 Lack of pervasive LT-HP metamorphism in the basement gneisses

The clockwise P-T path at HT-LP granulite facies conditions (Figs. 10, 11) retrieved for the anatectic gneisses is among the first to be documented in the Godhra-Chhota Udepur sector. The

path is similar to those retrieved for similar rocks in the CGC and the SMB crustal domains in the CITZ (summarised in Banerjee et al., 2021). LA-ICP-MS U-Pb (Zircon) dating by Banerjee et al. (2022b) and in the accompanying article (Banerjee et al., 2022a) demonstrates that this high-grade metamorphism in the anatectic gneisses occurred during the Late Paleoproterozoic (1.7–1.6 Ga). This P-T path is distinct from the Early Neoproterozoic clockwise P-T path with low-T, high-P peak metamorphic conditions recorded in the supracrustal rocks (Fig. 8e). But the P-T paths in the anatectic gneisses do not record the overprinting effects of the younger Early Neoproterozoic LT-HP path in the closely associated supracrustal rocks (Fig. 9b) in the tectonic mélange. However, sporadic occurrences of randomly oriented fibrolites of chlorite, phengitic micas and rare paragonite replacing biotite-cordierite-plagioclase assemblages (Fig. 2e) indicate that the basement gneisses experienced the D2-L2 low-T metamorphic effects, but compelling evidence for the overprinting effects of the low-T metamorphism induced by the Early Neoproterozoic crustal thickening in the anatectic basement gneisses is lacking.

The HT-LP metamorphism in the ~1.65 Ga basement gneisses predates the Early Neoproterozoic LT-HP metamorphic event by at least 600 million years, and therefore, the basement anatectic gneisses are likely to have cooled sufficiently prior to being re-metamorphosed at the lower temperature. This implies that the decompression paths in the ~1.65 Ga gneisses and the 1.03–0.93 Ga supracrustal rocks were not time equivalent, and instead the decompression paths are two distinct metamorphic events separated by ~600 million years. It also stands to reason that LT-HP metamorphic over-printing in the gneisses would require the stabilization of hydrous minerals at the expense of high-T anhydrous minerals. “Dry” high-grade rocks in the middle to lower crust are mechanically strong (Jackson et al., 2004), and cratons can sustain large stresses in continental collision zones (Yang et al., 2020). In such cratonic rocks,

the stabilization of low-T hydrous minerals is likely to be facilitated if crustal weakening is induced by fluid infusion (Jamtveit et al., 2018) and/or grain size reduction (Yang et al., 2020) as in zones of high shear strain. Jamtveit et al. (2018) demonstrate that the Caledonian eclogites formed at the expense of the Proterozoic granulites in the Bergen Arc (western Norway) due to pressure perturbations and fluid-induced weakening of the stressed lower crust; the authors conclude that the eclogitization was not the result of burial metamorphism alone. Following their argument, we suggest that the lack of D2 axial planar fabric in the gneisses and the absence of fabric-defining low-T hydrous minerals (vis-à-vis paucity of fluids) are likely to have contributed to the unresponsive nature of the high-grade rocks to the Early Neoproterozoic low-T metamorphic event in the older gneisses. Another factor that may have contributed to the passivity of the basement gneisses to the Early Neoproterozoic hydration event is the preferential partitioning of D2 strain in the rheologically weak supracrustal rocks (dominated by weak to shear mica schists and meta-carbonate rocks) interleaved with the mechanically strong older high-grade gneisses. Grain size reduction and enhanced fluid mobility are expected to be high in the gneisses in and adjoining the gneiss-supracrustal rock contacts and the gneisses; such structurally weak locales are likely to best exhibit retrograde overprinting. It is possible that such high-D2 strain locales within the anatectic gneisses, if preserved, could not be identified during the course of this study. Hence, stronger imprints of stabilization of low-T hydrous minerals in the gneisses remain undocumented.

1.3 Dynamics of accretion

For a comprehensive reconstruction of the dynamics of accretion between ADFB and CITZ, the inferences in this work are integrated with those in earlier studies (Banerjee et al.,

2021, 2022b) and in the accompanying article (Banerjee et al., 2022a) in the Godhra-Chhota Udepur sector. The important evidences are: (a) The D2 (thrust-dominated) and D3 (wrench-dominated) deformations constitute a progression in NNE-SSW crustal shortening that resulted in orogen-parallel stretching (Banerjee et al., 2022a, b). (b) The top-to-the-south thrust dominated D2 deformation (Banerjee et al., 2022a, b) and crustal thickening (~1.0 Ga) recorded in the supracrustal rocks (this study) led to the juxtaposition of the 1.7–1.6 Ga high-grade anatectic basement gneisses of the CITZ with the ~2.5 Ga foliated granitoids similar in age to the Berach granite and its chronological equivalents in the ADFB (accompanying article; Banerjee et al., 2022a). (c) The lack of Late Paleoproterozoic high-grade metamorphism in the ~2.5 Ga ADFB foliated granites and the absence of Archean dates in the Late Paleoproterozoic CITZ gneisses suggests the two terranes (ADFB-CITZ) were tectonically accreted at ~1.0 Ga (Banerjee et al., 2022a, b). (d) The accretion was associated with the post-D2 to syn-D3 the emplacement of extensive S-type granitoids at 0.95–0.93 Ga (Banerjee et al., 2022a, b). (e) The syn-D3 trains and imbrications among euhedral K-feldspar phenocrysts and the common occurrence of chess-board sub-grain microstructure in quartz grains (Banerjee et al., 2022a, b; Mamtani and Greiling, 2005) suggest that the deformation in the granitoids occurred at high-T and persisted during and outlasted the emplacement of the granitoids. (f) The granitoid emplacements culminated with the nucleation of basement piercing E-striking steep-dipping D3 transpressional shear zones (Banerjee et al., 2022a, b). (g) No evidence of post-D2 extension-related structural features were observed during investigation in and around 450 field stations we visited in the GC sector. (h) ~0.95 Ga granitoids are not as yet reported within the Lunavada Group of low-grade metamorphic rocks north of the GC sector.

The profusion of post-D2, syn-D3 Early Neoproterozoic syn-collisional S-type granitoids (Banerjee et al., 2022a, b) emplaced in the thickened accretion zone in excess of ~40 km needs to be explained. Additionally, some of the granitoids were deformed (D3) when hot, although the deformation outlasted granitoid emplacement. These features have also been noted in the Chottanagpur Gneiss Complex (Sequeira et al., 2020, 2021) far to the east (Fig. 1a) of the present study area, within the CITZ. Clearly, there needs to be a mechanism that would initiate melting in the basement gneisses and induce ascent of voluminous granitoids in the absence of demonstrable crustal extension. We ascribe the features to a subduction polarity reversal (*Willett, and Beaumont, 1994;* Wang et al., 2015). In this process, the crustal thickening occurred during the initial phase of northward subduction of the CITZ below the ADFB lithologies in the north (Fig. 12). We suggest this led to the interleaving of the CITZ gneisses dominant in the south with the Archean basement rocks equivalent to PGC-I in the ADFB to the north (accompanying article; Banerjee et al., 2022a).

In the next step, the expansive emplacement of 0.95–0.93 Ga S-type granitoids (Banerjee et al., 2022a) in the thickened crust in a down-going plate needs to be explained. The emplacement of these granitoids would require elevated temperatures at the source region of the granitoids. We suggest, following *Willett, and Beaumont (1994), that the* delamination of the down-going CITZ slab during continued crustal convergence led to the initiation of melting. But slab delamination broadly contemporaneous with crustal shortening would necessitate a reversal in the subduction polarity, i.e. the over-ridden CITZ plate evolved into an over-riding plate. Slab-delamination and south-directed subduction in its wake caused top-to-the-south thrusting of the supracrustal rocks and parts of the ADFB domain, and asthenospheric upwelling triggered melting of the tectonically interleaved CITZ and the ADFB lithologies (Fig. 12). The crustally-

derived melts ascended along a network of orogen-parallel post-D2 to syn-D3 channels (D3 transpressional shear zones) through a feed-back relationship between melt localisation and strain partitioning in a rheologically heterogeneous partially molten crust experiencing shortening (Brown and Solar, 1999; Bhadra et al., 2007; Jamieson et al., 2007). Experimental studies and theoretical considerations (Vigneresse et al., 1996) suggest that difference in the dynamic viscosity in a partially molten crust is likely to vary in excess of several orders of magnitude. Strain-induced by crustal shortening would be preferentially partitioned within the magma-bearing zones (cf. Vigneresse and Tikoff, 1999) and assist in magma ascent and nucleation of the D3 shear zones. This would explain the flow-textured granitoids deformed at supra-solidus conditions (Banerjee et al. 2022a, b): the crustal shortening event outlasted granitoid emplacement, and the deformation continued at sub-solidus state in the D3 granitoids, the supracrustal rocks and the basement gneisses.

2. CONCLUDING REMARKS

The results of this study integrated with those of Banerjee et al. (2021, 2022a, b) provide a regional tectonic framework for CITZ-ADFB accretion based on a large body of new structural, chronological, geochemical and metamorphic data that did not exist before from the crucial Godhra-Chhota Udepur sector. The tectonic restoration model proposed here is based on the findings in the Precambrian rocks exposed in the Godhra-Chhota Udepur sector. However, the veracity of the proposed model needs to be corroborated from an analysis of superposed deformations and kinematics of mesoscale structures, robust geochronology and quantitative metamorphic phase equilibrium analyses of critical rocks in the Lunavada Group of the ADFB

exposed in the north of the GC sector (this study). Towards this end, the model proposed in this study, and the first of its kind, provides a framework for future investigations.

Acknowledgements

This work constitutes a part of the Doctoral dissertation of the first author. The author acknowledges the Indian Institute of Technology Kharagpur for providing her with fellowship for the work. We put on record the help provided by Debarun Dutta in organising the initial fieldwork in the areas neighboring Godhra and Chhota Udepur during the pandemic. NS acknowledges the School of Earth, Ocean and Atmospheric Sciences, Goa University for the collaborative work. EPMA analyses were performed using the Science and Engineering Research Board (SERB) funded (IRPHA grant no. IR S4/ESF-16/2009) National Facility in the Department of Earth Sciences, Indian Institute of Technology Bombay (India). PN acknowledges financial support through a Core Research Grant (CRG grant no. CRG/2019/000812) by the SERB. The manuscript was greatly benefitted from the incisive comments and the observations of two anonymous journal reviewers. We acknowledge the Editorial handling of the manuscript by Nadia Malaspina.

APPENDIX

A. Mineral chemistry

Mineral chemical analyses were carried out with a CAMECA SX-FIVE Electron Probe Microanalyzer at the Department of Earth Sciences, IIT Bombay (India). The analyses were performed using an accelerating voltage of 15 kV with a beam current of 20 nA. The elements (Si K_a, Ti K_a, Al K_a, Fe K_a, Mg K_a, Mn K_a, Na K_a, Ca K_a, K K_a, P K_a, Zn K_a, and Ba L_a) were

calibrated using Natural and synthetic mineral standards. Matrix absorption corrections were performed using the X-PHI method (Merlet, 1992). The peak and background counts were measured for 20 s and 10 s, respectively. The overlap correction of Ba L_a on Ti K_a was corrected using the CAMECA Peak Sight software (version 6.1).

B. Whole rock geochemistry

Whole rock major element analyses of samples AW 142A [Figs. (2a, 3b, d, and 7a)] and AW 44 (Supplementary Material[3]) was performed at ACME Lab, Bureau Veritas, Vancouver, Canada. The protocol is listed in Appendix C of the accompanying article (Banerjee et al., 2022a).

The bulk rock composition for sample AW 372 (Fig. 2b, 7b, c) was analyzed by inductively coupled plasma atomic emission spectrometry (ICP-AES; SPECTRO-ARCOS simultaneous ICP) at the Sophisticated Analytical Instrument Facility, IIT Bombay. The rock chips were cleaned and powdered to a grain size of <75 µm with a HERZOG pulverizing mill. The powders of lithium metaborate (0.75 g) and lithium tetraborate (0.50 g) were mixed with 0.25 g of rock power in a platinum crucible, and fused at 1050 °C for 10 minutes in a muffle furnace. On cooling to 800 °C, the ignited mixture was transferred to a 100 ml glass beaker containing 80 ml of 1N HCl solution. After dissolving completely, the samples and standards were diluted (10 times) and transferred to a 100 ml volumetric flask. The instrument calibration was performed using the USGS reference materials (SDC-1, BIR-1, BHVO-2, BCR-2, GSP-2, RGM-2). Standard AGV-2 was run as an unknown to monitor drift in the instrument during analyses. Loss on ignition (LOI) values were estimated by heating rock powders at 950 °C for 10 minutes, then after cooling down to room temperature in a desiccator.

Figure captions

Fig. 1: (a) Structural-lithological map of the Godhra-Chhota Udepur sector. Localities discussed in the text are indicated. Inset shows the location of the study area within the Great India Proterozoic Fold Belt (GIPFOB). CGC: Chottanagpur Gneiss Complex; SMB-Satpura Mobile Belt; ADFB: Aravalli Delhi Fold Belt; CITZ: Central Indian Tectonic Zone. Axial plane foliation (S2) and fold axes and stretching lineations (L2) correspond to D2 deformation, and similarly for S3, L3 and D3. Locations of samples used in this study are in white-circle (add AW as prefix). (b) 3-dimensional cartoon showing the overall structural setting of the GC sector.

Fig. 2: Back-scattered electron (BSE) images of melanocratic gneisses; (a) leucosome-melanosome pairs in AW 142A, and (b) mineral-textural relations in the melanocratic mosaic in AW 372. Fabrics corresponding to D1a and D1b deformations are shown. Mineral abbreviations used are according to Whitney and Evans (2010), unless otherwise specified. White boxes correspond to the blown up images alongside. Close up images and X-ray element maps are shown in black boxes; the figure numbers of the close up images are keyed to the boxes. (7a), (7b) and (7c) keyed to boxes correspond to garnets for which X-ray element maps are provided in Fig. 7(a, b and c). (c) BSE image of cordierite within leucosome. (d) BSE image of sillimanite fibrolite within garnet. (e) BSE image of white mica-paragonite-chlorite fibrolite replacing cordierite-plagioclase aggregates. (f) Crossed polar image of mineral inclusion trails (S1a) in garnet. (g) Plane polarized light image of small idioblastic garnet in biotite aggregates. (h) Crossed polar image of sillimanite-defined inclusion trails in cordierite porphyroblast.

Fig. 3: Field photographs of anatectic gneisses (a–d) and supracrustal rocks (e–g). Melanocratic biotite-rich gneisses: (a) D2 top-to-the-south thrusting. (b) Interference patterns of D1a, D1b and D2 folds; note the occurrence of garnet porphyroblasts (arrow) in folded D1a leucosome layers (sample AW 142A). (c) Superposition of gently-inclined D2 folds and upright D3 folds (d) Profile section of W-trending open upright gently plunging folds (sample AW 142A). Supracrustal rocks: (e) Gently-inclined D2 folds in micaceous quartzites. (f) Gently-plunging D3 folds preserved in W-striking steep-dipping D3 high strain zone in metacarbonate rock. (g) Asymmetric D2 folds in mica schist being transposed locally to D3 shear zones.

Fig. 4: Textures in supracrustal rocks. (a, b) Crossed polar images (AW 70B) of talc (Tlc) - tremolite (Tr) aggregates defining D3 fabric in fine-grained recrystallized mosaic of calcite (Cal), dolomite (Dol) and quartz (Qz). In (a) note the occurrence of isolated kaolinite (Kln) grain in the mosaic. In (b) note the sieve-textured tremolite overgrowing the Tlc-Tr aggregates defining the D3 fabric. (c, d) Crossed polar images (AW 157B) of clinopyroxene (Cpx), talc (Tlc) associated with recrystallized calcite (Cal) and dolomite (Dol). Elliptical to round aggregates (arrow) of mono-mineralic polycrystalline serpentine (Srp) grains (within calcite-dolomite aggregates) possibly occurring as pseudomorphs of forsterite (not observed). (e, f) Plane polarized and crossed polar images showing D2 and D3 fabrics in amphibolite (Amp) (AW 45) defined by amphiboles (tschermakite and actinolite in composition), intimately associated with clinozoisite (Czo), plagioclase (Pl) and quartz. Calcite is rare or absent in the amphibolites.

Fig. 5: (a, b) Photomicrographs of mica schist (AW 46B) showing (a) inter-relationship between D2 and D3 schistosity defined white mica (Ms)-chlorite (Chl)-clinozoisite (Czo)

aggregates, (b) occurrence of pre-D2 schistosity in quartz microlithons, and (c) occurrence of post-D3 clinozoisite. (d, e) Compositions of white mica are plotted in Fe+Mg vs Si and Si vs. Al plots and compared with phengite reported from different high-P terrains (Velde, 1967; Kurata and Banno, 1974; Coombs et al., 1976; Dempster, 1992; Chopin, 1984; Banno, 1993; Itaya and Fukui, 1993; Carswell et al., 2000; Miyashita an Itaya, 2002; Ishwar-Kumar et al., 2013; Park et al., 2020; Ren et al., 2021). (f) BSE image and X-ray element maps of Al. Si, Fe and K in mica schist AW 46B. Arrow heads show the location of white micas.

Fig. 6: (a) Photomicrograph of the xenoblastic garnet porphyroblast in relation to D2 and D3 fabrics in mica schist AW 91. (b) X-ray element images of Ca, Mg, Fe and Mn of the garnet grain. (c) Rim to rim variations in the composition of the garnet along the line shown in the Mg element map.

Fig. 7: Chemical variations in garnet porphyroblasts in anatectic gneisses AW 142A, 372. X-ray element maps of Fe, Mn. Mg and Ca and compositional profiles of garnet along line A-A′ in (a) AW 142A, and (b, c) AW 372. Locations of of garnet (a) is shown in Fig. 2a, and for garnets in (b, c) shown in Fig. 2b. X_{Fe} [= Fe/(Fe + Mg + Mn + Ca)] and similarly for X_{Mn}, X_{Mg} and X_{Ca} in garnets.

Fig. 8: Results of thermo-barometry and P-T estimates: (a) mica schists (AW 91, 46), (b) amphibolite (AW 45), (c, d) anatectic gneisses (c: AW 142A, d: AW 372). The broken line in (a) is the P-T path obtained from NCKFMASHTi P-T pseudosection analyses in a white mica-chlorite schist (Fig. 9). The broken lines in (c, d) are the P-T paths obtained from Mn-NCKFMASH P-T pseudosections in the two anatectic gneisses (Figs. 10b, 11b). (e) Comparison of pre-D2 P-T conditions in the gneisses and the D2-D3 P-T

conditions in the mica schist. In the figures, the Al_2SiO_5 phase diagram and the minimum melting curve for granite are shown for reference only.

Fig. 9: P-T path reconstruction in white mica-chlorite schist AW 44 (mineral chemical data in Fig. 6a-c and Tables 1, 2). (a) NCKFMASHTi pseudosection in the P-T window 2–20 kbar and 450–650 °C. The white box is the outline for the phase assemblages of interest in AW 44 in (b). (b) In the NCKFMASHTi P-T pseudosection constructed in the P-T window 5–15 kbar, 410–550 °C, the contours of Si content (apfu) in white mica, albite content in plagioclase and X_{Fe}^{Chl} = Fe/(Fe+Mg) are shown. The bold broken line is the suggested clockwise P-T path experienced by the rock. The peak P-T conditions (white box) obtained from the mineral thermo-barometer in Fig. 8a is shown for reference. (c) NCKFMASH pseudosection in the P-T window 5–15 kbar, 410–550 °C, the contours of Si content (apfu) in white mica, albite content in plagioclase and X_{Fe}^{Chl} = Fe/(Fe+Mg) are shown. Note the similarity of the phase field in (b) and (c).

Fig. 10: (a) Mn-NCKFMASHTi and (b) Mn-NCKFMASH P-T pseudosection reconstructions in the anatectic gneiss AW 142A (mineral chemical data in Fig. 7a and Supplementary Material[4] in the P-T window 4.6–7 kbar and 660–820 °C. The contours of $X_{Ca,}$ X_{Mg} and X_{Fe} in garnet vol% of melt, garnet and cordierite are shown. The volume% ilmenite is shown in (a). Star represents the P-T conditions for the formation of garnet core composition. In (b) the prograde path, the peak conditions and the post-peak P-T path are shown by the broken line.

Fig. 11: (a) Mn-NCKFMASHTi and (b) Mn-NCKFMASH P-T pseudosection reconstructions in the anatectic gneiss AW 372 (mineral chemical data in Fig. 7b and Supplementary Material[6]) in the P-T window 4.6–7 kbar and 660–820 °C. The contours of $X_{Ca,}$ X_{Mg} and

X_{Fe} in garnet, and the contours of vol% of melt, garnet and cordierite are shown. Volume % of ilmenite is shown in (a). In (b) the prograde path, the peak conditions and the post-peak P-T path are shown by the broken line.

Fig. 12: Tectonic cartoon modified after Wang et al. (2015) is a possible reconstruction of the final geometry of the 1.0–0.95 Ga accretion zone evolved due to the convergence of Aravalli Delhi Fold Belt and the Central Indian Tectonic Zone. The inference is based on the observations made in this study and those in the accompanying article (Banerjee et al., 2022a) at the Godhra-Chhota Udepur sector.

Table caption

Table 1: Electron probe micro analytical data and structural formula of selected white mica (and quartz for reference only) in mica schists (AW 46B, AW 82A and AW 91).

Table 2: Electron probe micro analytical data and structural formulae of biotite [11(O, OH, F, Cl) basis], chlorite [14(O) basis], clinozoisite [12.5(O) basis] and plagioclase [8(O) basis] for samples AW 46B and AW 91 and garnet [8 (O) basis] in AW 91.

Table 3: Electron probe micro analytical data and structural formula of selected white mica (and quartz for reference only), chlorite plagioclase, clinozoisite and ilmenite in mica schist AW 44.

Supplementary Material

Supplementary Material[1]: Electron probe micro-analytical data and structural formulae of tremolite [24 (O) basis], dolomite [6 (O) basis], quartz [4 (O) basis], chlorite [14 (O) basis], talc [11 (O) basis], kaolinite [7 (O) basis], apatite [26 (O) basis] in the

metacarbonate sample AW 70B and clinopyroxene [6 (O) basis], serpentine [7 (O) basis], biotite [11 (O, OH, F, Cl) basis] in metacarbonate sample AW 157B. For calcite and dolomite only electron probe micro-analytical data has been provided for both the samples.

Supplementary Material[2]: Electron probe micro-analytical data and structural formulae of sphene [5 (O) basis], clinoamphibole [24 (O) basis], chlorite [14 (O) basis], plagioclase [8(O) basis], quartz [4 (O) basis], epidote [12.5 (O) basis] in the amphibolite sample AW 45.

Supplementary Material[3]: Back-scatter electron image of mica schist sample AW 44. (a) Thin-section scale back scatter electron image of the mica schist sample showing D3 crenulations on D2 schistosity. Note the paucity of Fe-Ti oxide phases in the sample. Close up images (b–d) are shown in black boxes; the figure numbers of the close up images are keyed to the boxes. (b, c) BSE image depicting inter-relationship between D1, D2 and D3 schistosity defined white mica (Ms)-chlorite (Chl) aggregates; note the occurrence of pre-D2 schistosity in the D2 intrafolial domain in (b). (d) Rare ilmenite (Ilm) and apatite (Ap) in the section. (e) Occurrence of clinozoisite (Czo) and sphene (Spn) in the section.

Supplementary Material[4]: Electron probe micro-analytical data and structural formulae of biotite, muscovite [both 11 (O, OH, F, Cl) basis], garnet [12 (O) basis], plagioclase [8(O) basis], sillimanite [5 (O) basis], cordierite [18 (O) basis], chlorite [14 (O) basis] and quartz [4 (O) basis] in anatectic gneiss AW 142A.

Supplementary Material[5]: Electron probe micro-analytical data and structural formulae of garnet [12(O) basis], biotite and muscovite [11(O, OH, F, Cl) basis], cordierite [18(O) basis],

chlorite [14(O) basis], plagioclase [8(O) basis], sillimanite [5(O)basis] and quartz [4(O)basis] for basement gneiss sample AW 372.

Supplementary Material[6]: Histograms of compositional parameters in biotite and plagioclase in AW 142A are shown.

References

Auzanneau, E., Schmidt, M. W., Vielzeuf, D., Connolly, J. D., 2010. Titanium in phengite: a geobarometer for high temperature eclogites. Contributions to Mineralogy and Petrology 159, 1. https://doi.org/10.1007/s00410-009-0412-7

Bakker, R. J., Mamtani, M. A., 2000. Fluid inclusions as metamorphic process indicators in the Southern Aravalli Mountain Belt (India). Contributions to Mineralogy and Petrology 139, 163–179. https://doi.org/10.1007/PL00007669

Banerjee, A., Sequeira, N., Bhattacharya, A. 2021. Tectonics of the Greater India Proterozoic Fold Belt, with emphasis on the nature of curvature of the belt in west-central India. Earth Science Reviews 221, 103758. https://doi.org/10.1016/j.earscirev.2021.

Banerjee, A., Cogne, N., Sequeira, N., Bhattacharya, A., 2022a. Dynamics of Early Neoproterozoic accretion, west-central India: I. Geochronology and Geochemistry. Lithos (accompanying article; https://doi.org/10.1016/j.lithos.2022.106715)

Banerjee, A., Sequeira, N., Naraga, P., Cogné, N., Bhattacharya, A., 2022b. Early Neoproterozoic tectonics in the Godhra – Chhota Udepur sector: Evidence for two-stage accretion in the Greater India Proterozoic Fold Belt (GIPFOB). Lithosphere https://doi.org/10.2113/2022/9322892

Banno, Y., 1993. Chromian sodic pyroxene, phengite and allanite from the Sanbagawa blueschists in the eastern Kii Peninsula, central Japan. Mineralogical Journal 16, 306–317. https://doi.org/10.2465/minerj.16.306

Bhadra, S., Bhattacharya, A., 2007. The barometer tremolite + tschermakite+ 2 albite= 2 pargasite+ 8 quartz: Constraints from experimental data at unit silica activity, with application to garnet-free natural assemblages. American Mineralogist 92, 491–502. https://doi.org/10.2138/am.2007.2067

Bhadra, S., Das, S., Bhattacharya, A., 2007. Shear zone-hosted migmatites (Eastern India): the role of dynamic melting in the generation of REE-depleted felsic melts, and implications for disequilibrium melting. Journal of Petrology 48, 435–457.

Bhattacharya, A., Mazumdar, A.C., Sen, S.K., 1988. Fe-Mg mixing in cordierite; constraints from natural data and implications for cordierite-garnet geothermometry in granulites. American Mineralogist 73, 338–344.

Bhattacharya, A., Mohanty, L., Maji, A., Sen, S. K., Raith, M., 1992. Non-ideal mixing in the phlogopite–annite binary: constraints from experimental data on Mg–Fe partitioning and a reformulation of the biotite–garnet geothermometer. Contributions to Mineralogy and Petrology 111, 87–93. https://doi.org/10.1007/BF00296580

Blundy, J. D., Holland, T. J., 1990. Calcic amphibole equilibria and a new amphibole-plagioclase geothermometer. Contributions to mineralogy and petrology 104, 208–224. https://doi.org/10.1007/BF00306444

Brown, M., Solar, G. S., 1999. The mechanism of ascent and emplacement of granite magma during transpression: A syntectonic granite paradigm. Tectonophysics 312, 1–33. https://doi .org /10 .1016 /S0040 -1951 (99) 00169 -9

Carswell, D. A., Wilson, R. N., Zhai, M. G., 2000. Metamorphic evolution, mineral chemistry and thermobarometry of schists and orthogneisses hosting ultra-high pressure eclogites in the Dabieshan of central China. Lithos 52, 121–155. https://doi.org/10.1016/S0024-4937(99)00088-2

Chopin, C., 1984. Coesite and pure pyrope in high-grade blueschists of the Western Alps: a first record and some consequences. Contributions to Mineralogy and Petrology 86, 107–118. https://doi.org/10.1007/BF00381838

Cibin, G., Cinque, G., Marcelli, A., Mottana, A., Sassi, R., 2008. The octahedral sheet of metamorphic 2 M 1-phengites: a combined EMPA and AXANES study. American Mineralogist 93, 414–425. https://doi.org/10.2138/am.2008.2548

Coggon, R., Holland, T. J. B., 2002. Mixing properties of phengitic micas and revised garnet-phengite thermobarometers. Journal of Metamorphic Geology 20, 683–696. https://doi.org/10.1046/j.1525-1314.2002.00395.x

Connolly, J. A., 2005. Computation of phase equilibria by linear programming: a tool for geodynamic modeling and its application to subduction zone decarbonation. Earth and Planetary Science Letters 236, 524–541. https://doi.org/10.1016/j.epsl.2005.04.033

Coombs, D. S., Nakamura, Y., Vuagnat, M., 1976. Pumpellyite-actinolite facies schists of the Taveyanne Formation near Loèche, Valais, Switzerland. Journal of Petrology 17, 440–471. https://doi.org/10.1093/petrology/17.4.440

Das, S., Singh, P. K., Sikarni, C., 2009. A preliminary study of thermal metamorphism in the Champaner Group of rocks in Panchmahals and Vadodara districts of Gujarat. Indian Journal of Geoscience 63, 373–382.

Dempster, T. J., 1992. Zoning and recrystallization of phengitic micas: implications for metamorphic equilibration. Contributions to Mineralogy and Petrology 109, 526–537. https://doi.org/10.1007/BF00306554

Ferry, J. M., Spear, F. S., 1978. Experimental calibration of the partitioning of Fe and Mg between biotite and garnet. Contributions to Mineralogy and Petrology 66, 113–117. https://doi.org/10.1007/BF00372150

Ganguly, J., Saxena, S. K., 1984. Mixing properties of aluminosilicate garnets: constraints from natural and experimental data, and applications to geothermo-barometry. American Mineralogist 69, 88–97.

Goscombe, B, Foster, D. A., Gray, D., Wade, B. Marsellos, A., 2017. Titus, J. 2017. Deformation correlations, stress field switches and evolution of an orogenic intersection: The Pan-African Kaoko-Damara orogenic junction, Namibia. Geoscience Frontiers 8, 1187–1232.

Green, T. H., Hellman, P. L., 1982. Fe-Mg partitioning between coexisting garnet and phengite at high pressure, and comments on a garnet-phengite geothermometer. Lithos 15, 253–266. https://doi.org/10.1016/0024-4937(82)90017-2

Heron, A.M., 1934. Geology of Aravalli Fold Belt. Memoirs of the Geological Survey of India 50–54.

Hodges, K.V., Spear, F.S., 1982. Geothermometry, geobarometry and the Al2SiO5 triple point at Mt Moosilauke, New Hampshire. American Mineralogist 67, 1118–1134.

Hodges, K. V., Crowley, P. T., 1985. Error estimation and empirical geothermobarometry for pelitic systems. American Mineralogist 70, 702–709.

Hoinkes, G., 1986. Effect of grossular-content in garnet on the partitioning of Fe and Mg between garnet and biotite—an empirical investigation on staurolite—zone samples from the Austroalpine Schneeberg complex. Contributions to Mineralogy and Petrology 92, 393–399. https://doi.org/10.1007/BF00572168

Hoisch, T. D., 1989. A muscovite-biotite geothermometer. American Mineralogist 74, 565–572.

Hoisch, T. D., 1990. Empirical calibration of six geobarometers for the mineral assemblage quartz+ muscovite+ biotite+ plagioclase+ garnet. Contributions to Mineralogy and Petrology 104, 225–234.

Holdaway, M. J., 2000. Application of new experimental and garnet Margules data to the garnet–biotite geothermometer. American Mineralogist 85, 881–892. https://doi.org/10.2138/am-2000-0701

Holdaway, M. J., Lee, S. M., 1977. Fe-Mg cordierite stability in high-grade pelitic rocks based on experimental, theoretical, and natural observations. Contributions to Mineralogy and Petrology 63, 175–198. https://doi.org/10.1007/BF00398778

Holdaway, M. J., Mukhopadhyay, B., Dyar, M. D., Guidotti, C. V., Dutrow, B. L., 1997. Garnet–biotite geothermometry revised: new Margules parameters and a natural specimen data set from Maine. American Mineralogist 82, 582–595. https://doi.org/10.2138/am-1997-5-618

Holland, T., Blundy, J., 1994. Non-ideal interactions in calcic amphiboles and their bearing on amphibole-plagioclase thermometry. Contributions to Mineralogy and Petrology 116, 433–447. https://doi.org/10.1007/BF00310910

Holland, T. I. M., Powell, R., 2001. Calculation of phase relations involving haplogranitic melts using an internally consistent thermodynamic dataset. Journal of Petrology 42, 673–683. https://doi.org/10.1093/petrology/42.4.673

Holness, M. B., 2018. Melt segregation from silicic crystal mushes: a critical appraisal of possible mechanisms and their microstructural record. Contributions to Mineralogy and Petrology 173**,** https://doi.org/10.1007/s00410-018-1465-2

Indares, A., Martignole, J., 1985. Biotite–garnet geothermometry in the granulite facies: the influences of Ti and Al in biotite. American Mineralogist 70, 272–278.

Ishwar-Kumar, C., Windley, B. F., Horie, K., Kato, T., Hokada, T., Itaya, T., Yagi, K., Gouzu, C., Sajeev, K., 2013. A Rodinian suture in western India: New insights on India-Madagascar correlations. Precambrian Research 236, 227–251. https://doi.org/10.1016/j.precamres.2013.07.023

Itaya, T., Fukui, S., 1994. Phengite K-Ar ages of schists from the Sanbagawa southern marginal belt, central Shikoku, southwest Japan: Influence of detrital mica and deformation on age. Island Arc 3, 48–58. https://doi.org/10.1111/j.1440-1738.1994.tb00004.x

Jackson, J.A. Austrheim, A., Mckenzie, D., Priestly, K., 2004. Metastability, material strength, and the support of mountain belts. Geology 32, 625–628.

Jamieson, R. A., Beaumont, C., Nguyen, M. H., Culshaw, N. G., 2007, Synconvergent ductile flow in variable strength continental crust: Numerical models with application to the western Grenville orogen: Tectonics. 26, TC5005. https:// doi .org /10 .1029 /2006TC00203

Jamtveit, B., Moulas, E., Andersen, T. B., Austrheim, H., Corfu, F., Petley-Ragan, A., Schmalholz, S. M., 2018. Nature Scientific Reports 8, 17011. https://doi.org/10.1038/s41598-018-35200-1.

Jolivet, L., Brun, J. P., 2010. Cenozoic geodynamic evolution of the Aegean. International Journal of Earth Sciences 99, 109–138.

Kaneko, Y., Miyano, T., 2004. Recalibration of mutually consistent garnet–biotite and garnet–cordierite geothermometers. Lithos 73, 255–269. https://doi.org/10.1016/j.lithos.2003.12.009

Koziol, A. M., 1989. Recalibration of the garnet-plagioclase-Al2SiO5-quartz (GASP) geobarometer and applications to natural processes. EOS 70, 493.

Koziol, A. M., Newton, R. C., 1988. Redetermination of the anorthite breakdown reaction and improvement of the plagioclase-garnet-Al2SiO5-quartz geobarometer. American Mineralogist, 73, 216–223.

Krogh, E. J., Råheim, A., 1978. Temperature and pressure dependence of Fe-Mg partitioning between garnet and phengite, with particular reference to eclogites. Contributions to Mineralogy and Petrology 66, 75–80. https://doi.org/10.1007/BF00376087

Kurata, H., Banno, S., 1974. Low-grade progressive metamorphism of pelitic schists of the Sazare area, Sanbagawa metamorphic terrain in central Sikoku, Japan. Journal of Petrology 15, 361–382. https://doi.org/10.1093/petrology/15.2.361

Kuster, D., Harms, U. 1998. Post-collisional potassic granitoids from the southern and northwestern parts of the Late Neoproterozoic East African Orogen: a review. Lithos 45, 177–195.

Leake, B. E., Woolley, A. R., Arps, C. E., Birch, W. D., Gilbert, M. C., Grice, J. D., Hawthorne, F. C., Kato, A., Kisch, H. J., Krivovichev, V. G., Linthout, K., 1997. Nomenclature of amphiboles; report of the Subcommittee on Amphiboles of the International Mineralogical Association Commission on new minerals and mineral names. Mineralogical Magazine 61, 295–310. https://doi.org/10.1180/minmag.1997.061.405.13

Mamtani, M. A., Greiling, R. O., 2005. Granite emplacement and its relation with regional deformation in the Aravalli Mountain Belt (India) inferences from magnetic fabric. Journal of Structural Geology 27, 2008–2023

Massonne, H. J., Schreyer, W., 1987. Phengite geobarometry based on the limiting assemblage with K-feldspar, phlogopite, and quartz. Contributions to Mineralogy and Petrology 96, 212–224. https://doi.org/10.1007/BF00375235

Meissner, R., Mooney, W., 1998. Weakness of the lower continental crust: a condition for delamination, uplift, and escape. Tectonophysics, 296, 47–60.

Merlet, C., 1992. Quantitative Electron Probe Microanalysis: New Accurate Φ (ρz) Description, In: Boekestein, A., Pavićević, M.K. (Eds.), Electron Microbeam Analysis. Springer Vienna, Vienna, 107–115.

Miyashita, A., Itaya, T., 2002. K-Ar age and chemistry of phengite from the Sanbagawa schists in the Kanto Mountains, central Japan, and their implication for exhumation tectonics. Gondwana Research 5, 837–848. https://doi.org/10.1016/S1342-937X(05)70917-5

Newton, R., Wood, B., Kleppa, O., 1981. Thermochemistry of silicate solid solutions. Bulletin De Mineralogie 104, 162–171. https://doi.org/10.3406/bulmi.1981.7451

Newton, R. C., Haselton, H. T., 1981. Thermodynamics of the garnet—plagioclase—Al 2 SiO 5—quartz geobarometer. In: Newton, R. C., Navrotsky, A., Wood, B. J. (Eds.) Thermodynamics of minerals and melts. Springer-Verlag, New York, 131–147. https://doi.org/10.1007/978-1-4612-5871-1_7

Park, C., Kim, N., Choi, S.J., Song, Y., 2020. Mg-Phengite in Carbonate Rock Syngenetically Formed from Hydrothermal Fluid: Micro-Textural Evidence and Mineral Chemistry. Minerals 10, 668. https://doi.org/10.3390/min10080668

Perchuk, L. L., 1981. Correction of the biotite–garnet thermometer in case of the Mn=Mg+Fe isomorphism in garnet. Doklady Geoscience Section 256, 72–73.

Perchuk, L. L., Lavrent'eva, I. V., 1983. Experimental investigation of exchange equilibria in the system cordierite–garnet–biotite. In: Saxena, S.K. (Ed.), Kinetics and Equilibrium in Mineral Reactions. Springer-Verlag, New York, 199–239. https://doi.org/10.1007/978-1-4612-5587-1_7

Perchuk, L. L., Aranovich, L. Y., Podlesskii, K. K., Lavrant'eva, I., Gerasimov, V. Y., Fed'Kin, V. V., Kitsul, V. I., Karsakov, L. P., Berdnikov, N. V., 1985. Precambrian granulites of the Aldan shield, eastern Siberia, USSR. Journal of Metamorphic Geology 3, 265–310. https://doi.org/10.1111/j.1525-1314.1985.tb00321.x

Powell, R., Evans, J. A., 1983. A new geobarometer for the assemblage biotite-muscovite-chlorite-quartz. Journal of Metamorphic Geology 1, 331–336. https://doi.org/10.1111/j.1525-1314.1983.tb00278.x

Ren, Y., Chen, D., Wang, H., Zhu, X., Bai, B., 2021. Grenvillian and early Paleozoic polyphase metamorphism recorded by eclogite and host garnet mica schist in the North Qaidam

orogenic belt. Geoscience Frontiers 12, 101170. https://doi.org/10.1016/j.gsf.2021.101170

Searle, M. P., Parrish, R. R., Hodges, K. V., Hurford, A., Ayres, M. W., Whitehouse, M. J., 1997. Shisha Pangma leucogranite, south Tibetan Himalaya: field relations, geochemistry, age, origin, and emplacement. Journal of Geology 105, 295–317.

Selverstone, J., Spear, F. S., 1985. Metamorphic P-T paths from pelitic schists and greenstones in the southwest Tauern Window, Eastern Alps. Journal of Metamorphic Geology 3, 439–465.

Sequeira, N., Mahato, S., Rahl, J., Sarkar, S., Bhattacharya, A., 2020. The anatomy and origin of a syn-convergent Grenvillian-age metamorphic core complex, Chottanagpur Gneiss Complex, Eastern India. Lithosphere. https://doi.org/10.2113/2020/8833404

Sequeira, N., Bhattacharya, A., Bell, E., 2021. The ~1.4 Ga A-type granitoids in the "Chottanagpur crustal block" (India), and its relocation from Columbia to Rodinia? Geoscience Frontiers. https://doi.org/10.1016/j.gsf.2020.12.017

Thompson, A. B., 1976. Mineral reactions in pelitic rocks; I, Prediction of PTX (Fe-Mg) phase relations. American Journal of Science 276, 401–424. https://doi.org/10.2475/ajs.276.4.425

Velde, B., 1967. Si+ 4 content of natural phengites. Contributions to Mineralogy and Petrology 14, 250–258. https://doi.org/10.1007/BF00376643

Vigneresse, J. L., Barbey, P., Cuney, M., 1996, Rheological transitions during partial melting and crystallization with application to felsic magma segregation and transfer. Journal of Petrology 37, 1579–1600. https://doi .org /10 .1093 /petrology /37 .6 .1579.

Waldbaum, D. R., Thompson Jr, J. B., 1968. Mixing properties of sanidine crystalline solutions: II. Calculations based on volume data. American Mineralogist 53, 2000–2017.

Wang, J., Kusky, T., Wang, L., Polat, A., Deng, H., 2015. A neoarchean subduction polarity reversal event in the North China Craton. Lithos 220, 133–146. doi.org/10.1016/j.lithos.2015.01.029

Wells, P. R. A., 1979. Chemical and thermal evolution of Archaean sialic crust, southern West Greenland. Journal of Petrology 20, 187–226. https://doi.org/10.1093/petrology/20.2.187

Wells, P. R. A., Richardson, S. W., 1979. Thermal evolution of metamorphic rocks in the Central Highlands of Scotland. Geological Society of London Special Publications 8, 339–344. https://doi.org/10.1144/GSL.SP.1979.008.01.37

White, R. W., Powell, R., Holland, T. J. B., 2007. Progress relating to calculation of partial melting equilibria for metapelites. Journal of metamorphic Geology 25, 511–527. https://doi.org/10.1111/j.1525-1314.2007.00711.x

White, R. W., Powell, R., Johnson, T. E., 2014. The effect of Mn on mineral stability in metapelites revisited: New a–x relations for manganese-bearing minerals. Journal of Metamorphic Geology 32, 809–828. https://doi.org/10.1111/jmg.12095

Whitney, D.L., Evans, B.W., 2010. Abbreviations for names of rock-forming minerals. American Mineralogist 95, 85–87. https://doi.org/10.2138/am.2010.3371

Willett, S. D., Beaumont, C., 1994. Subduction of Asian lithospheric mantle beneath Tibet inferredfrom models of continental collision. Nature. 369, 642–645. https://doi.org/10.1038/369642a0

Williams, M. L., Grambling, J. A., 1990. Manganese, ferric iron, and the equilibrium between garnet and biotite. American Mineralogist 75, 886–908.

Yang, J., Kaus, B. J. P., li, Y., Leloup, P. H., Popov, A. A., Lu, G., Wang, K., Zhao, L., 2020. Lower crustal rheology controls the development of large offset strike-slip faults during the Himalayan-Tibetan orogeny. Geophysical Research Letters 47. https://doi.org/10.1029/2020GL089435

Table 1: Electron probe micro-analytical data and structural formulae of phengitic micas [11(O,OH,F,Cl) basis] and quartz [4(O) basis] from sample AW 46B, AW 91 and AW 82A

	AW 46B							AW 91							AW 82A						
	Ph	**Ph**	**Ph**	**Ph**	**Ph**	**Ph**	**Qz**	**Ph**	**Ph**	**Ph**	**Ph**	**Ph**	**Ph**	**Qz**	**Ph**	**Ph**	**Ph**	**Ph**	**Ph**	**Ph**	**Qz**
SiO_2	46.6	47.5	47.5	46.9	47.8	48.8	99.8	47.9	48.3	48.0	48.9	46.5	47.0	99.3	46.8	47.2	47.0	47.6	47.4	46.7	10.6
TiO_2	0.44	0.48	0.44	0.51	0.47	0.44	bdl	0.40	0.29	0.23	0.26	0.50	0.40	0.02	0.21	0.24	0.15	0.57	0.51	0.23	bdl
Al_2O_3	34.7	33.8	28.7	32.0	30.4	30.5	bdl	31.6	32.2	32.6	32.1	31.3	30.3	0.19	33.7	33.8	33.4	32.5	31.6	34.1	0.01
Cr_2O_3	0.00	0.00	0.00	0.00	bdl	bdl	bdl	0.00	bdl	0.00	bdl	0.00	0.00	bdl	–	–	–	–	–	–	–
FeO	3.07	3.02	4.23	4.02	4.90	4.76	0.02	3.67	2.97	2.60	2.85	2.84	2.30	0.88	2.81	3.02	2.90	3.56	2.64	3.12	bdl
MnO	0.02	0.03	0.01	bdl	0.02	bdl	bdl	bdl	bdl	bdl	0.02	0.02	bdl	0.15	–	–	–	–	–	–	–
MgO	0.64	0.92	1.87	1.13	1.67	1.78	0.01	1.97	1.68	1.57	1.80	1.52	1.52	0.02	0.92	0.99	0.97	1.27	1.33	0.84	0.01
CaO	bdl	bdl	0.08	0.11	0.02	bdl	0.02	0.06	0.01	0.05	bdl	0.03	bdl	0.08	bdl	bdl	bdl	bdl	bdl	bdl	0.01
Na_2O	1.01	0.68	0.22	0.45	0.38	0.50	bdl	0.30	0.42	0.30	0.24	0.22	0.39	bdl	0.32	0.33	0.35	0.35	0.27	0.34	bdl
K_2O	9.88	10.2	10.0	8.98	10.2	10.3	0.01	10.1	10.7	10.7	10.9	10.0	10.7	bdl	10.7	10.8	10.6	10.5	10.4	10.6	0.03
BaO	0.36	0.37	0.26	0.32	0.32	0.31	bdl	0.22	0.21	0.20	0.18	0.15	0.21	bdl	–	–	–	–	–	–	–
ZnO	bdl	bdl	0.05	bdl	bdl	bdl	0.01	0.05	bdl	bdl	bdl	bdl	bdl	bdl	–	–	–	–	–	–	–
P_2O_5	0.01	bdl	bdl	bdl	bdl	bdl	0.04	bdl	bdl	bdl	0.02	bdl	bdl	bdl	0.02	0.01	bdl	bdl	0.04	bdl	bdl
Total	**96.7**	**96.9**	**93.4**	**94.5**	**96.2**	**97.4**	**99.9**	**95.7**	**96.5**	**96.3**	**97.3**	**92.8**	**92.8**	**99.4**	**95.5**	**96.5**	**95.4**	**96.4**	**95.2**	**96.0**	**10.6**
Si	3.08	3.13	3.27	3.17	3.21	3.23	1.00	3.21	3.20	3.18	3.21	3.20	3.24	0.99	3.13	3.13	3.15	3.16	3.18	3.11	1.00
Ti	0.02	0.02	0.02	0.03	0.02	0.02	0.00	0.02	0.01	0.01	0.01	0.01	0.02	0.00	0.01	0.01	0.01	0.03	0.08	0.01	0.00
Al	2.71	2.62	2.33	2.55	2.40	2.38	0.00	2.45	2.50	2.55	2.49	2.53	2.46	0.00	2.66	2.64	2.63	2.55	2.50	2.68	0.00
Cr	0.00	0.00	0.00	0.00	0.00	0.00	0.00	0.00	0.00	0.00	0.00	0.00	0.00	0.00	–	–	–	–	–	–	–
Fe^{2+}	0.17	0.17	0.24	0.23	0.28	0.26	0.00	0.21	0.16	0.14	0.16	0.16	0.13	0.01	0.16	0.17	0.16	0.20	0.15	0.17	0.00
Mn	0.00	0.00	0.00	0.00	0.00	0.00	0.00	0.00	0.00	0.00	0.00	0.00	0.00	0.00	–	–	–	–	–	–	–

Mg	0.06	0.09	0.19	0.11	0.17	0.18	0.00	0.20	0.17	0.16	0.18	0.16	0.16	0.00	0.09	0.10	0.10	0.13	0.13	0.08	0.00
Ca	0.00	0.00	0.01	0.01	0.00	0.00	0.00	0.00	0.00	0.00	0.00	0.00	0.00	0.00	0.00	0.00	0.00	0.00	0.00	0.00	0.00
Na	0.13	0.09	0.03	0.06	0.05	0.06	0.00	0.04	0.05	0.04	0.03	0.03	0.05	0.00	0.04	0.04	0.04	0.05	0.03	0.04	0.00
K	0.83	0.86	0.88	0.77	0.88	0.86	0.00	0.87	0.90	0.91	0.91	0.88	0.94	0.00	0.91	0.91	0.91	0.89	0.89	0.90	0.00
Zn	0.02	0.02	0.01	0.02	0.02	0.02	0.00	0.01	0.01	0.01	0.01	0.01	0.01	0.00	–	–	–	–	–	–	–
Ba	0.00	0.00	0.00	0.00	0.00	0.00	0.00	0.00	0.00	0.00	0.00	0.00	0.00	0.00	–	–	–	–	–	–	–
P	0.00	0.00	0.00	0.00	0.00	0.00	0.00	0.00	0.00	0.00	0.00	0.00	0.00	0.00	0.00	0.00	0.00	0.00	0.00	0.00	0.00
Σcation	**7.03**	**7.00**	**6.99**	**6.94**	**7.03**	**7.02**	**1.00**	**7.00**	**7.01**	**7.00**	**7.00**	**6.98**	**7.00**	**1.01**	**7.01**	**7.01**	**7.00**	**7.00**	**6.96**	**7.01**	**1.00**

bdl-below detection limit

Table 2: Electron probe micro-analytical data and structural formulae of biotite [11(O, OH, F, Cl) basis], chlorite [14(O) basis], garnet [8 (O) basis], epidote [12.5(O) basis] and plagioclase [8(O) basis] for samples AW 46B and AW 91

	AW 46B							AW 91							
	Bt	**Chl**	**Chl**	**Ep**	**Ep**	**Pl**	**Pl**	**Grt core**	**Grt rim**	**Bt**	**Bt**	**Chl**	**Chl**	**Pl**	**Pl**
SiO_2	39.1	25.4	25.8	37.8	37.6	68.5	68.2	37.0	37.8	38.8	37.9	24.9	26.7	68.0	67.1
TiO_2	2.21	0.05	0.09	0.12	bdl	0.02	0.01	0.09	0.03	1.51	1.64	0.06	0.06	bdl	bdl
Al_2O_3	16.7	20.4	21.1	23.1	23.3	19.5	19.7	20.8	21.4	17.7	17.7	20.7	20.5	20.0	20.4
Cr_2O_3	0.11	bdl	0.03	0.05	0.08	0.01	0.01	0.04	bdl	bdl	0.08	0.06	0.01	bdl	bdl
Fe_2O_3	–	–	–	12.8	13.0	–	–	–	–	–	–	–	–	–	–
FeO	19.4	25.1	25.1	11.5	11.7	0.12	0.05	29.6	31.5	20.1	20.7	28.8	27.4	0.09	0.26
MnO	0.12	0.24	0.29	0.40	0.26	bdl	bdl	5.34	3.17	0.12	0.16	0.49	0.46	bdl	bdl
MgO	9.76	14.0	14.6	0.01	0.03	bdl	bdl	1.49	1.77	8.61	8.63	11.3	11.7	bdl	0.06
CaO	0.64	0.06	0.02	23.7	23.3	0.16	0.29	5.55	5.59	0.38	0.28	0.02	0.21	0.71	0.33
Na_2O	0.17	0.02	0.03	0.01	bdl	12.5	12.4	0.06	0.03	0.09	0.09	0.01	0.01	12.2	11.7
K_2O	7.13	0.06	0.04	bdl	bdl	0.06	0.09	bdl	0.03	7.94	8.20	0.03	0.47	0.10	0.46
BaO	bdl	bdl	bdl	bdl	0.04	0.03	bdl	0.01	bdl	bdl	bdl	bdl	bdl	bdl	bdl
ZnO	0.06	0.00	0.00	0.02	bdl	bdl	bdl	0.04	0.07	0.05	0.03	bdl	0.19	bdl	bdl
P_2O_5	bdl	bdl	bdl	bdl	bdl	0.01	bdl	0.05	0.04	bdl	bdl	0.01	0.02	0.01	bdl
Total	**95.4**	**85.3**	**87.0**	**96.8**	**96.3**	**101.1**	**100.8**	**100.0**	**101.5**	**95.4**	**95.4**	**86.4**	**87.7**	**101.1**	**100.2**
Si	2.91	2.75	2.73	3.01	3.01	2.97	2.97	2.99	3.00	2.91	2.87	2.72	2.85	2.95	2.94

Ti	0.12	0.00	0.01	0.01	0.00	0.00	0.00	0.01	0.00	0.09	0.09	0.01	0.00	0.00	0.00
Al	1.47	2.61	2.64	2.17	2.19	1.01	1.01	1.98	2.00	1.56	1.57	2.67	2.58	1.03	1.05
Cr	0.01	0.00	0.00	0.00	0.01	0.00	0.00	0.00	0.00	0.00	0.00	0.00	0.00	0.00	0.00
Fe^{3+}	–	–	–	0.82	0.84	–	–	–	–	–	–	–	–	–	–
Fe^{2+}	1.21	2.27	2.23	–	–	0.00	0.00	2.00	2.09	1.26	1.30	2.64	2.45	0.00	0.01
Mn	0.01	0.02	0.03	0.03	0.02	0.00	0.00	0.37	0.21	0.01	0.01	0.05	0.04	0.00	0.00
Mg	1.09	2.26	2.30	0.00	0.00	0.00	0.00	0.18	0.21	0.96	0.97	1.84	1.86	0.00	0.00
Ca	0.05	0.01	0.00	2.02	1.99	0.01	0.01	0.48	0.47	0.03	0.02	0.00	0.02	0.03	0.02
Na	0.02	0.00	0.01	0.00	0.00	1.06	1.05	0.01	0.00	0.01	0.01	0.00	0.00	1.03	0.99
K	0.68	0.01	0.01	0.00	0.00	0.00	0.00	0.00	0.00	0.76	0.79	0.00	0.06	0.01	0.03
Zn	0.00	0.00	0.00	0.00	0.00	0.00	0.00	0.00	0.00	0.00	0.00	0.00	0.00	0.00	0.00
Ba	0.00	0.00	0.00	0.00	0.00	0.00	0.00	0.00	0.00	0.00	0.00	0.00	0.01	0.00	0.00
P	0.00	0.00	0.00	0.00	0.00	0.00	0.00	0.00	0.00	3E-04	0.001	0.00	0.00	0.00	0.00
Σcation	**7.57**	**9.94**	**9.94**	**8.06**	**8.06**	**5.05**	**5.05**	**8.01**	**8.00**	**7.61**	**7.65**	**9.94**	**9.88**	**5.05**	**5.04**

bdl-below detection limit

Table 3: Electron probe micro-analytical data and structural formulae of phengitic micas [11(O,OH,F,Cl) basis], quartz [4(O) basis, chlorite [14(O) basis], garnet [8 (O) basis], epidote [12.5(O) basis], plagioclase [8(O) basis], ilmenite [3(O) basis], sphene [5(O) basis] and apatite [26(O) basis] for mica schist sample AW 44

	D3 Mica	**D3 Mica**	**D3 Mica**	**D3 Mica**	**D3 Mica**	**D3 Mica**	**D2 Mica**	**D2 Mica**	**D2 Mica**	**D2 Mica**	**D2 Mica**	**D2 Mica**	**D2 Mica**	**Ilm**	**Ilm**	**Pl**	**Chl**	**Chl**	**Chl**	**Chl**	**Sph**	**Ep**	**Qtz**	**Qtz**	**Ap**
SiO_2	48.80	48.81	48.83	47.79	48.80	47.79	50.00	49.92	49.96	49.91	49.97	49.93	48.89	0.02	0.01	64.16	24.22	25.22	24.17	25.18	30.13	37.78	98.95	98.77	0.02
TiO_2	0.41	0.31	0.34	0.44	0.31	0.29	0.16	0.27	0.25	0.20	0.36	0.27	0.19	51.2	50.8	bdl	0.05	0.05	0.10	0.08	35.85	0.13	0.01	bdl	bdl
Al_2O_3	34.46	33.34	33.32	34.43	32.77	33.31	30.09	31.13	31.18	31.14	32.24	32.23	31.10	0.03	0.01	22.11	21.19	21.12	21.18	21.17	1.88	27.85	0.03	0.03	0.01
Cr_2O_3	0.03	0.04	0.08	0.03	bdl	0.00	0.08	bdl	0.08	bdl	0.01	0.02	bdl	bdl	bdl	bdl	bdl	bdl	0.02	bdl	0.01	0.01	0.04	bdl	0.06	bdl
F	–	–	–	–	–	–	–	–	–	–	–	–	–	–	–	–	–	–	–	–	–	–	6	–	–	–

Fe_2O_3	2.05	2.33	2.48	2.14	3.73	2.14	2.78	3.01	2.65	3.26	2.66	2.62	2.77	41.8344	42.6333	0.18	28.22	28.22	28.55	27.55	0.44	6.24.93	0.26	0.10	0.12
FeO														.0300	.7000							.1000			
MnO	bdl	0.03	0.03	0.02	0.05	0.01	bdl	0.01	bdl	0.01	bdl	0.05	0.02	0.06	0.01	bdl	0.33111.6	0.39122.2	0.36111.9	0.28111.2	0.05	0.03	bdl	bdl	bdl
MgO	0.98	1.27	1.22	1.06	1.91	1.15	1.88	1.84	1.78	1.71	1.44	1.53	1.82	0.06	0.01	bdl	3.12	0.05	0.03	0.15	0.04	23.16	bdl	bdl	bdl
CaO	bdl	bdl	0.02	0.03	0.02	0.00	bdl	0.04	0.02	0.03	0.05	0.03	bdl	0.03	0.08	10.510	0.01	bdl	bdl	bdl	0.01	0.01	bdl	bdl	bdl
Na_2O	0.43	0.55	0.41	0.46	0.35	0.38	0.34	0.44	0.40	0.38	0.26	0.36	0.44	bdl	bdl	0.03	bdl	bdl	bdl	bdl	0.18	0.04	0.01	0.02	0.05
K_2O	10.1	9.98	9.83	9.96	9.24	9.80	10.00	9.91	9.89	10.0	9.67	9.73	10.3	bdl	0.010	bdl	bdl	bdl	bdl	bdl	bdl	bdl	bdl	bdl	bdl
BaO	0.28	0.26	0.24	0.29	0.24	0.22	0.20	0.19	0.23	0.18	0.22	0.21	0.17	bdl	bdl	bdl	bdl	bdl	bdl	bdl	bdl	bdl	bdl	bdl	bdl
ZnO	0.01	bdl	0.02	0.01	bdl	0.00	bdl	bdl	0.04	bdl	0.02	bdl	0.04	0.18	0.18	0.05	0.08	bdl	0.040	0.06	0.010	bdl	bdl	bdl	bdl
P_2O_5	0.01	bdl	bdl	0.03	bdl	0.00	bdl	bdl	bdl	0.03	bdl	bdl	bdl	bdl	bdl	bdl	bdl	bdl	0.02	bdl	0.010	0.07	bdl	0.02	41.83
F	0.02	0.08	0.03	0.05	0.04	0.02	0.04	0.11	0.09	0.07	0.04	0.10	0.17	bdl	bdl	0.01	bdl	bdl	bdl	bdl	0.58	bdl	bdl	bdl	.5000
Cl	bdl	0.01	0.01	0.02	bdl	0.02	bdl	bdl	0.01	0.02	bdl	0.01	bdl	bdl	bdl	bdl	bdl	0.01	0.01	0.01	bdl	bdl	bdl	bdl	0.01
Total	**97.0**	**96.4**	**96.2**	**96.8**	**96.6**	**95.2**	**96.3**	**96.3**	**96.9**	**96.4**	**96.9**	**96.5**	**95.8**	**97.4**	**97.5**	**100.7**	**86.6**	**87.4**	**87.5**	**86.8**	**97.5**	**95.4**	**98.8**	**98.9**	**100.3**
Si	3.14	3.17	3.19	3.14	3.16	3.19	3.29	3.25	3.25	3.25	3.25	3.24	3.26	0.0001	0.000	2.8400	2.6300	2.7100	2.6600	2.7700	1.0100	3.090	2.000	2.000	0.000
Ti	0.02	0.02	0.02	0.02	0.02	0.01	0.01	0.01	0.01	0.01	0.02	0.01	0.01	.0	.9	.0	.0	.0	.0	.0	.9	.0	.0	.0	.0

Al	2.67	2.60	2.58	2.65	2.55	2.60	2.40	2.44	2.46	2.45	2.50	2.50	2.43	0.000	0.000	0.000	0.000	0.000	0.000	0.000	0.000	0.690	0.000	0.000	0.000	0.000
Cr	0.000	0.000	0.000	0.000	0.000	0.000	0.000	0.000	0.000	0.000	0.000	0.000	0.000	0.000	0.000	0.140	0.000	0.000	0.000	0.000	0.000	0.070	0.000	0.000	0.000	0.000
Fe^{3+}	–	–	–	–	–	–	–	–	–	–	–	–	–	–	–	–	–	–	–	–	–	0.043	–	–	–	–
Fe^{2+}	0.111	0.113	0.114	0.112	0.121	0.112	0.115	0.117	0.115	0.118	0.115	0.114	0.115	0.910	0.930	0.810	2.570	2.540	2.570	2.470	0.010	–	0.000	0.000	0.000	0.020
Mn	0.000	0.000	0.000	0.000	0.000	0.000	0.000	0.000	0.000	0.000	0.000	0.000	0.000	0.000	0.080	0.000	0.031	0.041	0.031	0.031	0.000	0.010	0.000	0.000	0.000	0.000
Mg	0.110	0.112	0.112	0.110	0.119	0.111	0.119	0.118	0.117	0.117	0.114	0.115	0.118	0.000	0.000	0.000	0.889	0.961	0.911	0.791	0.000	0.000	0.000	0.000	0.000	0.000
Ca	0.000	0.000	0.000	0.000	0.000	0.000	0.000	0.000	0.000	0.000	0.000	0.000	0.000	0.000	0.000	0.000	0.000	0.000	0.000	0.000	0.001	0.023	0.000	0.000	0.000	0.010
Na	0.006	0.007	0.005	0.006	0.004	0.005	0.004	0.006	0.005	0.003	0.003	0.005	0.006	0.000	0.000	0.900	0.000	0.000	0.000	0.000	0.000	0.000	0.000	0.000	0.000	0.000
K	0.885	0.884	0.883	0.883	0.878	0.883	0.884	0.884	0.883	0.885	0.881	0.882	0.888	0.000	0.000	0.010	0.010	0.010	0.000	0.010	0.010	0.000	0.000	0.000	0.000	0.010
Ba	0.001	0.001	0.001	0.001	0.001	0.001	0.001	0.001	0.001	0.001	0.001	0.001	0.001	0.000	0.000	0.000	0.000	0.000	0.000	0.000	0.000	0.000	0.000	0.000	0.000	0.000
Zn	0.000	0.000	0.000	0.000	0.000	0.000	0.000	0.000	0.000	0.000	0.000	0.000	0.000	0.000	0.000	0.000	0.000	0.000	0.000	0.000	0.000	0.000	0.000	0.000	0.000	0.006
P	0.000	0.000	0.000	0.000	0.000	0.000	0.000	0.000	0.000	0.000	0.000	0.000	0.000	0.000	0.000	0.000	0.000	0.000	0.000	0.000	0.000	0.000	0.000	0.000	0.000	0.240
Σcation	**6.965**	**6.967**	**6.944**	**6.955**	**6.966**	**6.963**	**6.944**	**6.966**	**6.944**	**6.966**	**6.960**	**6.922**	**6.988**	**2.000**	**2.001**	**5.044**	**9.966**	**9.955**	**9.955**	**9.855**	**3.044**	**8.266**	**2.000**	**2.000**	**16.16**
X_{Na}	–	–	–	–	–	–	–	–	–	–	–	–	–	–	–	0.85	–	–	–	–	–	–	–	–	–	–
X_{Mg}	–	–	–	–	–	–	–	–	–	–	–	–	–	–	–	–	0.44	0.44	0.44	0.44	–	–	–	–	–	–

	2 4 3 2

bdl: below detection limit

Declaration of interests

☒The authors declare that they have no known competing financial interests or personal relationships that could have appeared to influence the work reported in this paper.

☐The authors declare the following financial interests/personal relationships which may be considered as potential competing interests:

Highlights

- ~1.65 Ga HT-LP clockwise granulite metamorphism in CITZ basement anatectic gneiss
- ~0.95 Ga LT-HP clockwise metamorphism in the CITZ allochthonous supracrustal rocks
- E-striking CITZ & N-striking Aravalli Delhi Fold Belt (ADFB) accreted at ~0.95 Ga
- ~0.95 Ga metamorphism coeval with crustal shortening and granitoid emplacement
- Early Neoproterozoic oblique accretion related to subduction polarity reversal

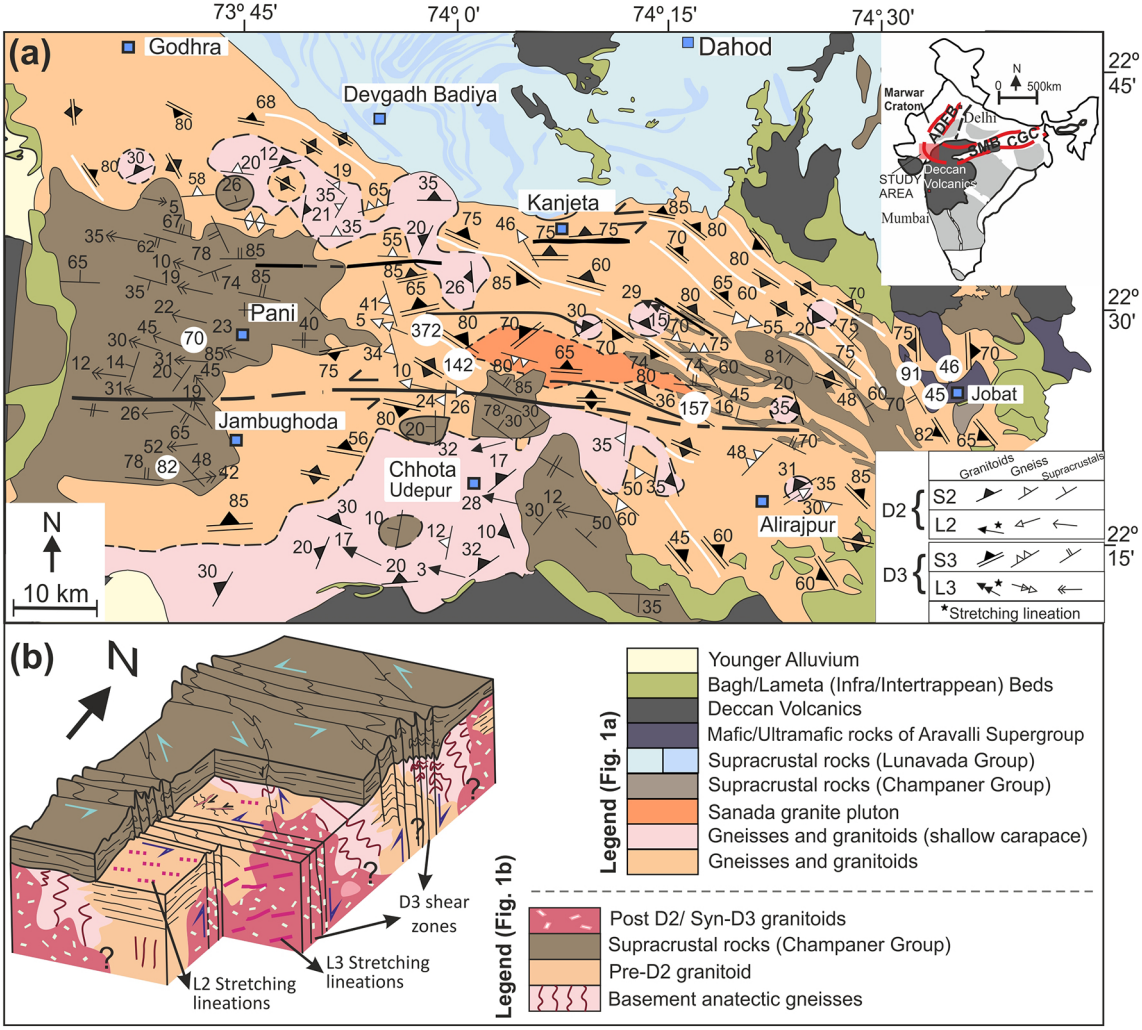
(a)
Godhra
Dahod
Devgadh Badiya
Kanjeta
Pani
Jambughoda
Chhota Udepur
Alirajpur
Jobat
73° 45'
74° 0'
74° 15'
74° 30'
22° 45'
22° 30'
22° 15'
N
10 km
Marwar Craton
Delhi
ADFB
CMB
CGC
Deccan Volcanics
STUDY AREA
Mumbai
0 500km
Granitoids
Gneiss
Supracrustals
D2
S2
L2
D3
S3
L3
*Stretching lineation
(b)
N
D3 shear zones
L3 Stretching lineations
L2 Stretching lineations
Legend (Fig. 1a)
Younger Alluvium
Bagh/Lameta (Infra/Intertrappean) Beds
Deccan Volcanics
Mafic/Ultramafic rocks of Aravalli Supergroup
Supracrustal rocks (Lunavada Group)
Supracrustal rocks (Champaner Group)
Sanada granite pluton
Gneisses and granitoids (shallow carapace)
Gneisses and granitoids
Legend (Fig. 1b)
Post D2/ Syn-D3 granitoids
Supracrustal rocks (Champaner Group)
Pre-D2 granitoid
Basement anatectic gneisses

Figure 1

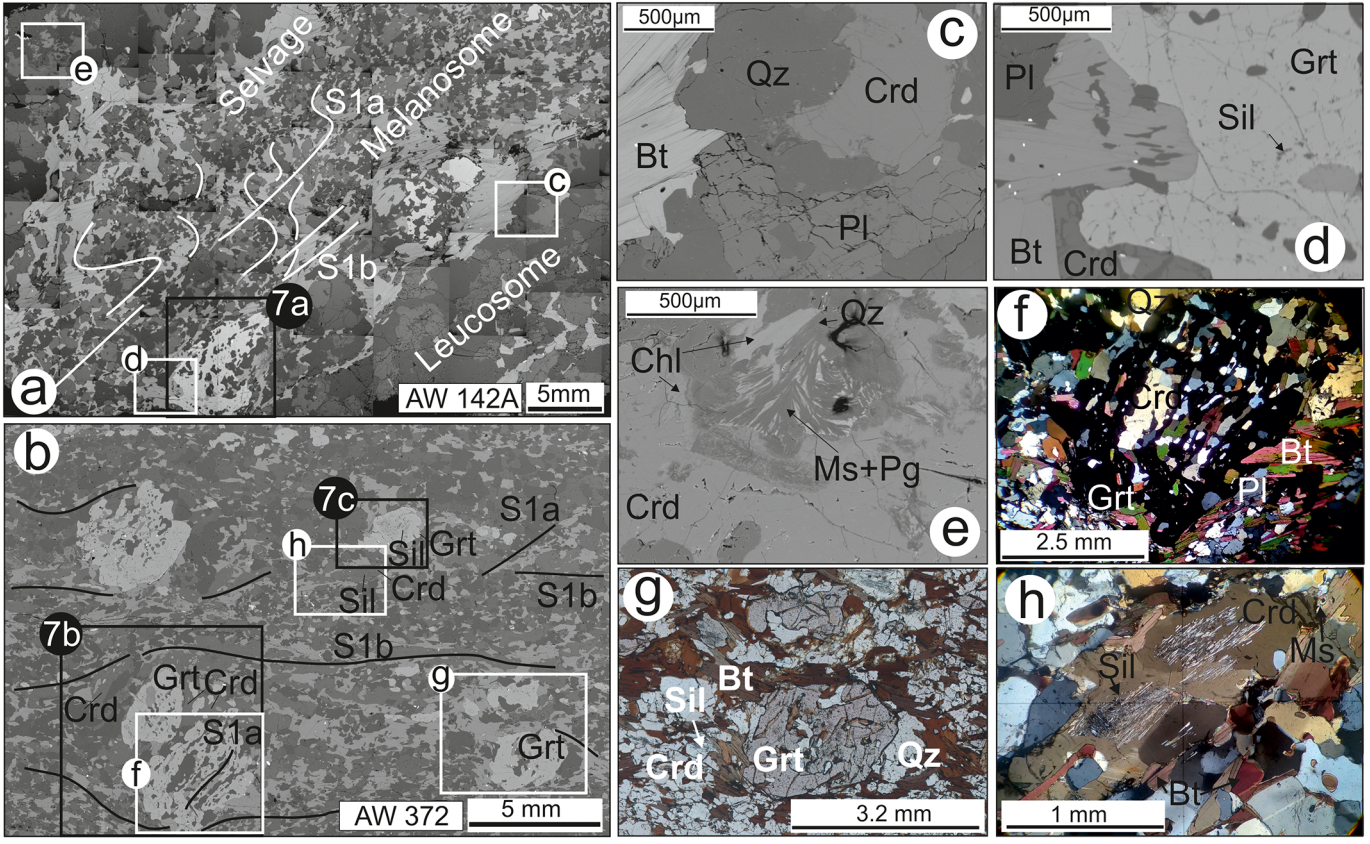
a
e
Selvage
S1a
Melanosome
c
S1b
7a
d
Leucosome
AW 142A
5mm
b
7c
h
Sil
Grt
S1a
Sil
Crd
S1b
7b
S1b
Grt
Crd
Crd
S1a
g
Grt
f
AW 372
5 mm
500µm
c
Qz
Crd
Bt
Pl
500µm
Pl
Grt
Sil
Bt
Crd
d
500µm
Qz
Chl
Ms+Pg
Crd
e
f
Qz
Crd
Bt
Grt
Pl
2.5 mm
g
Bt
Sil
Crd
Grt
Qz
3.2 mm
h
Crd
Sil
Ms
Bt
1 mm

Figure 2

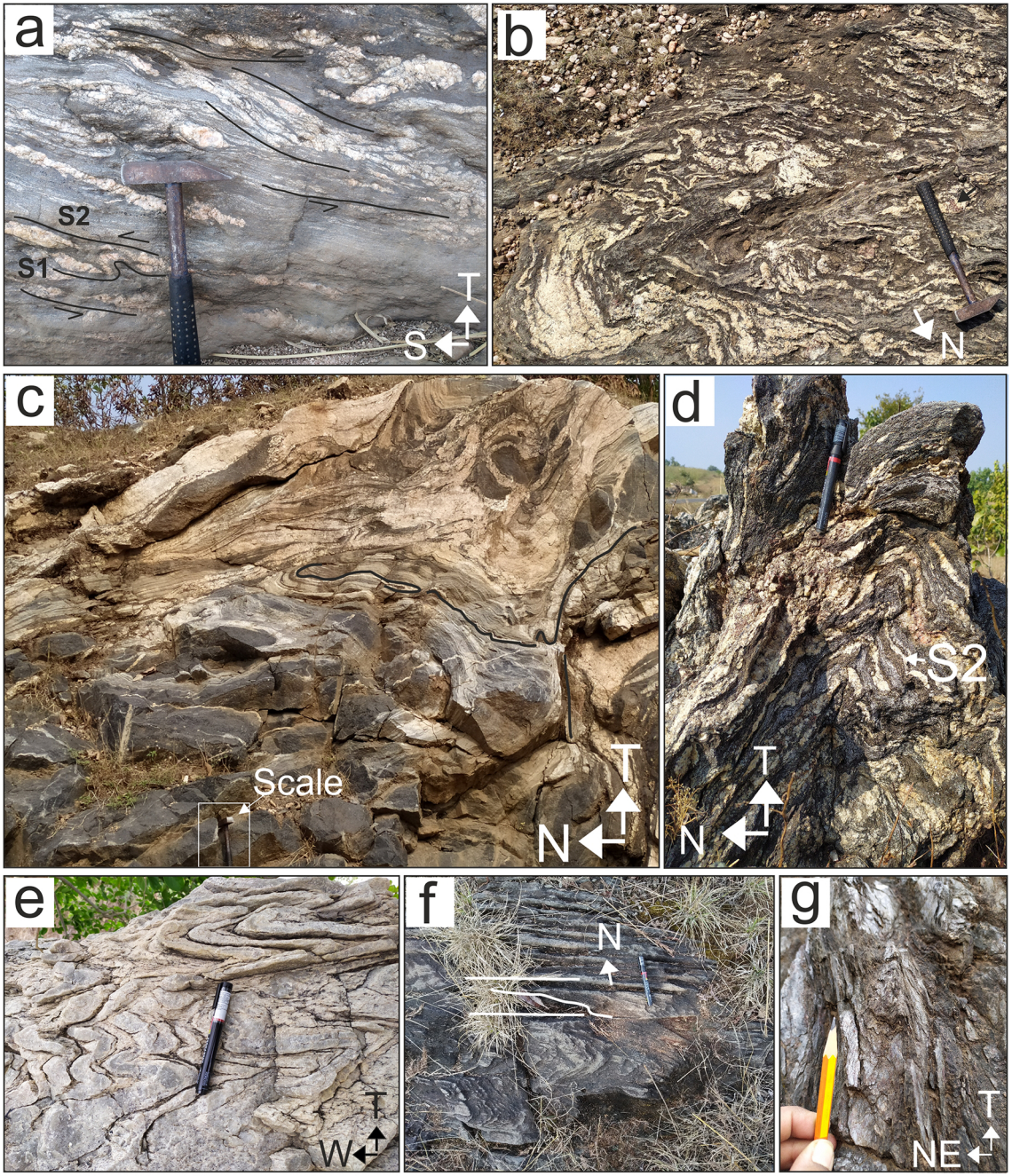

Figure 3

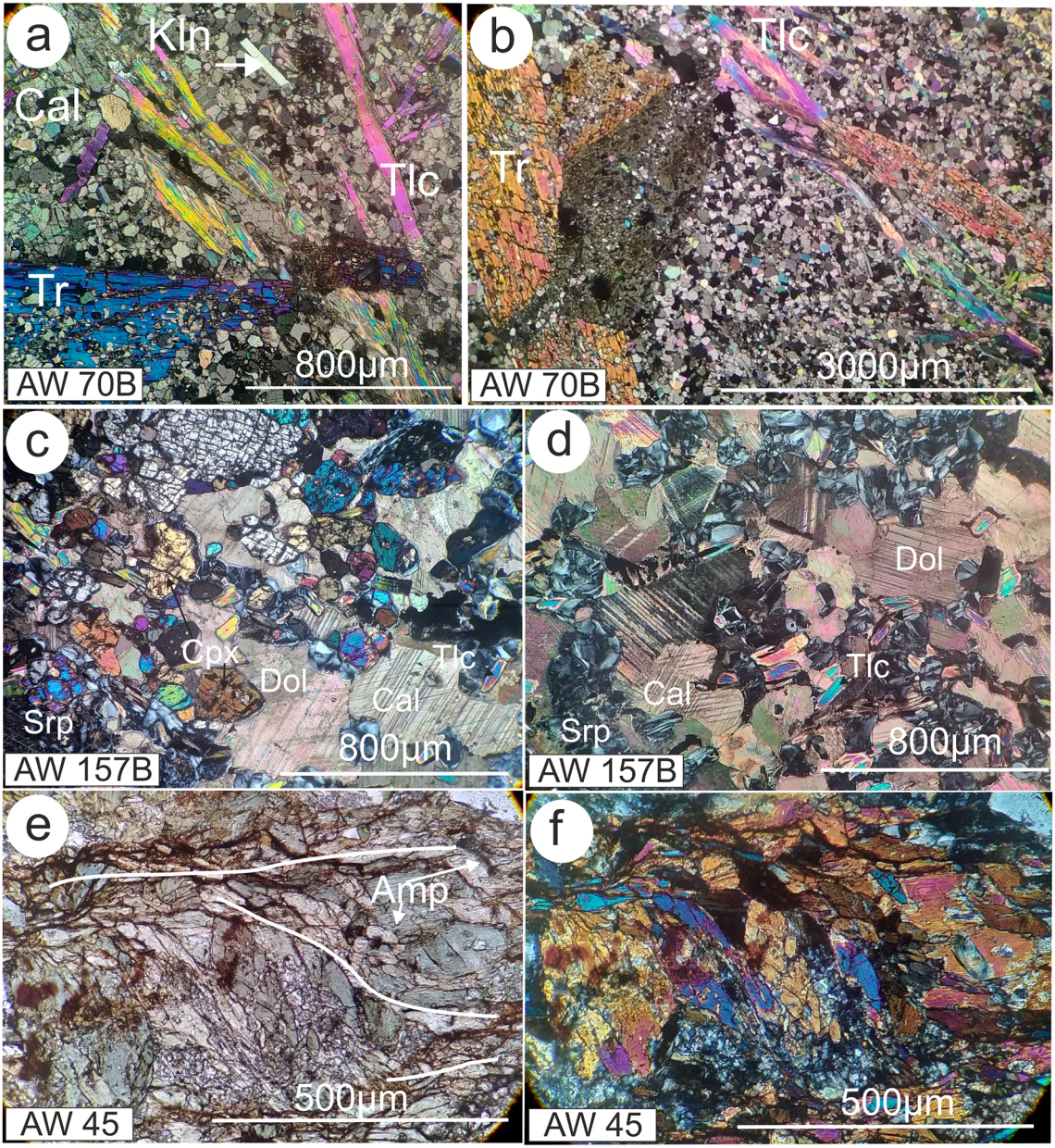
a
Kln
Cal
Tlc
Tr
800µm
AW 70B
b
Tlc
Tr
3000µm
AW 70B
c
Cpx
Dol
Tlc
Cal
Srp
800µm
AW 157B
d
Dol
Tlc
Cal
Srp
800µm
AW 157B
e
Amp
500µm
AW 45
f
500µm
AW 45

Figure 4

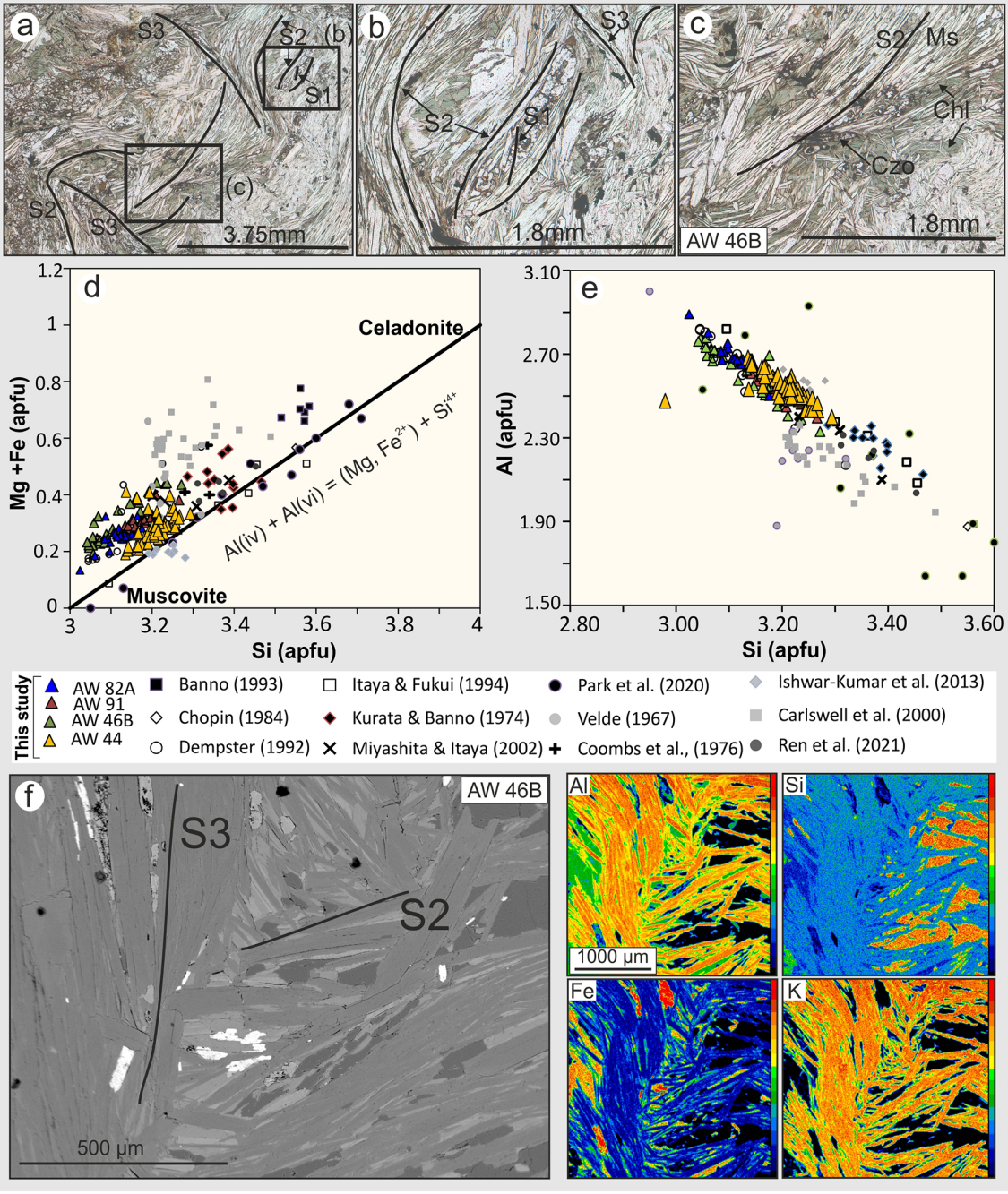
a
S3
S2
(b)
S1
(c)
S2
S3
3.75mm
b
S3
S2
S1
1.8mm
c
S2
Ms
Chl
Czo
AW 46B
1.8mm
d
Celadonite
Muscovite
Al(iv) + Al(vi) = (Mg, Fe2+) + Si4+
Mg +Fe (apfu)
Si (apfu)
e
Al (apfu)
Si (apfu)
This study
AW 82A
AW 91
AW 46B
AW 44
Banno (1993)
Chopin (1984)
Dempster (1992)
Itaya & Fukui (1994)
Kurata & Banno (1974)
Miyashita & Itaya (2002)
Park et al. (2020)
Velde (1967)
Coombs et al., (1976)
Ishwar-Kumar et al. (2013)
Carlswell et al. (2000)
Ren et al. (2021)
f
AW 46B
S3
S2
500 µm
Al
Si
1000 µm
Fe
K

Figure 5

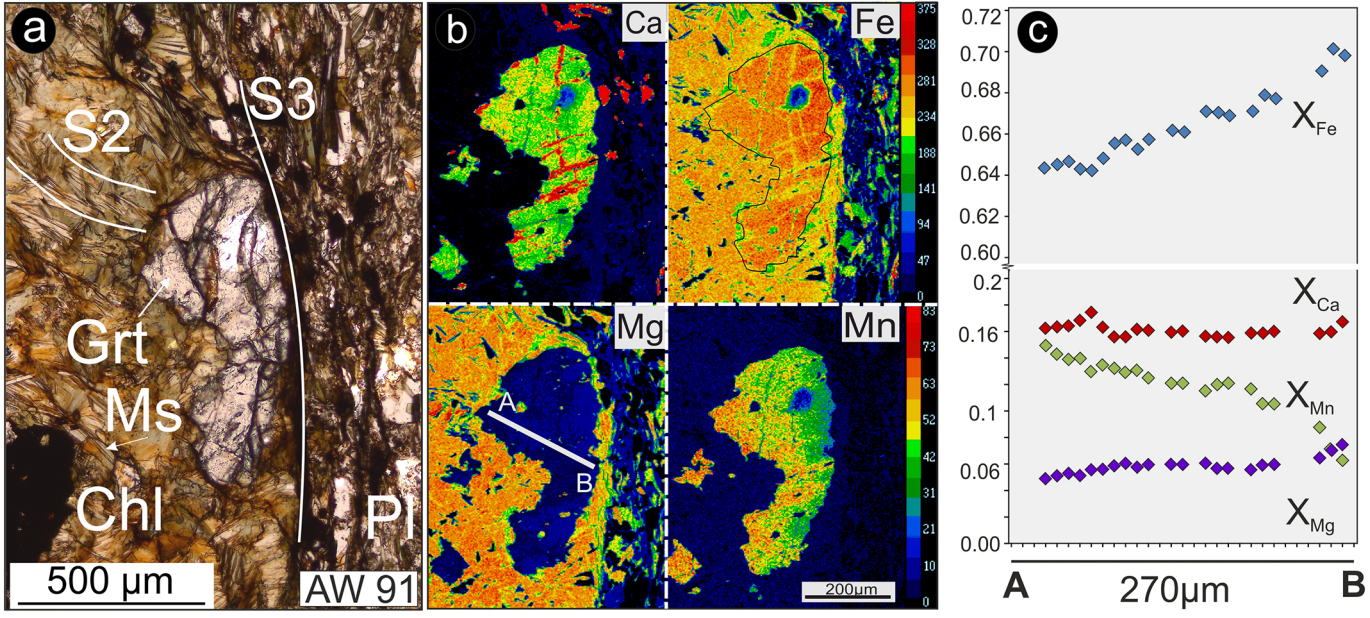
a
S2
S3
Grt
Ms
Chl
Pl
500 µm
AW 91
b
Ca
Fe
Mg
Mn
A
B
200µm
375
328
281
234
188
141
94
47
0
83
73
63
52
42
31
21
10
0
c
0.72
0.70
0.68
0.66
0.64
0.62
0.60
0.2
0.16
0.1
0.06
0.00
X_{Fe}
X_{Ca}
X_{Mn}
X_{Mg}
A
270µm
B

Figure 6

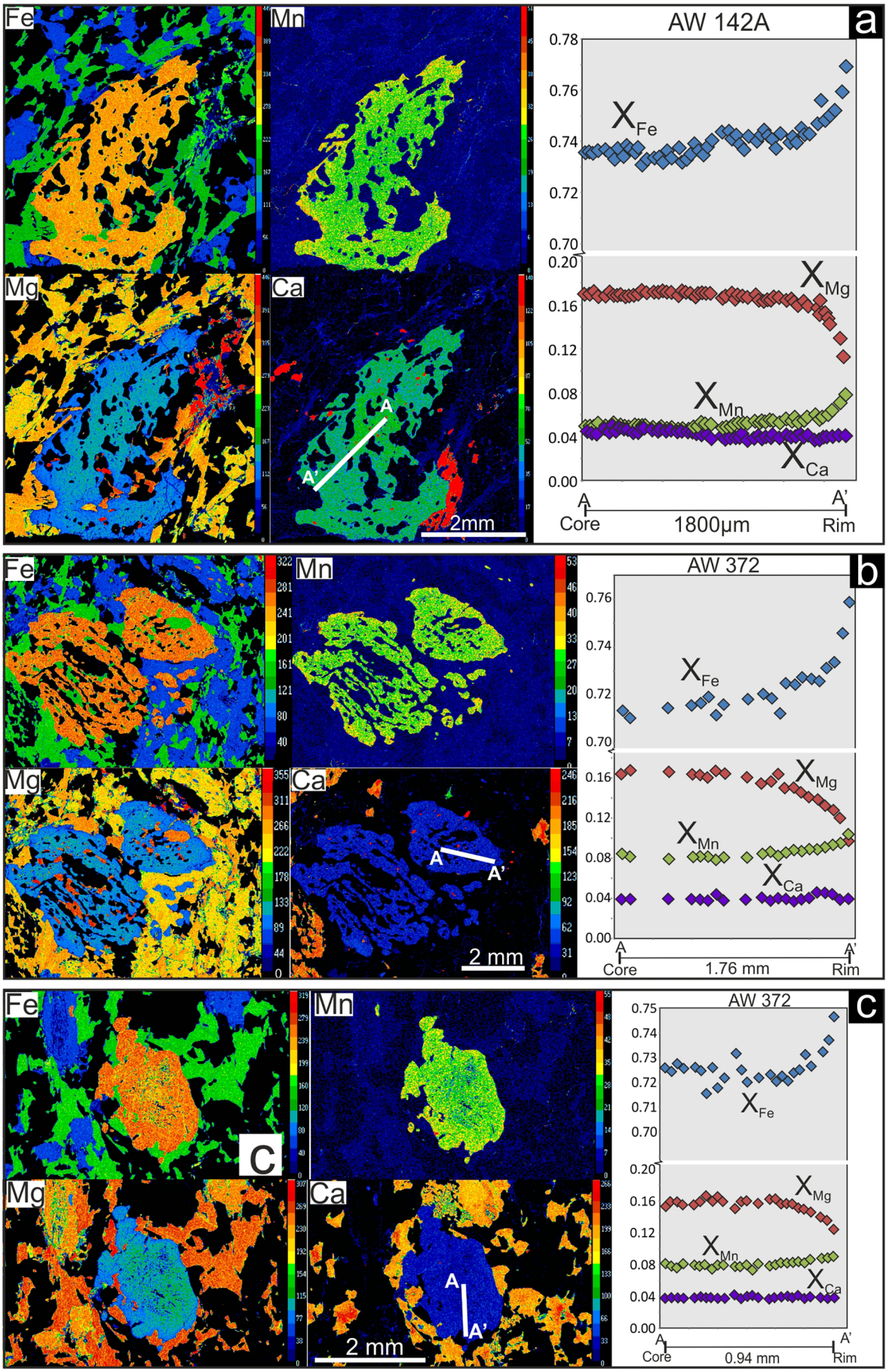
a
AW 142A
Fe
Mn
Mg
Ca
A
A'
2mm
X_{Fe}
X_{Mg}
X_{Mn}
X_{Ca}
0.78
0.76
0.74
0.72
0.70
0.20
0.16
0.12
0.08
0.04
0.00
Core
1800µm
Rim
b
AW 372
2 mm
1.76 mm
c
AW 372
0.94 mm

Figure 7

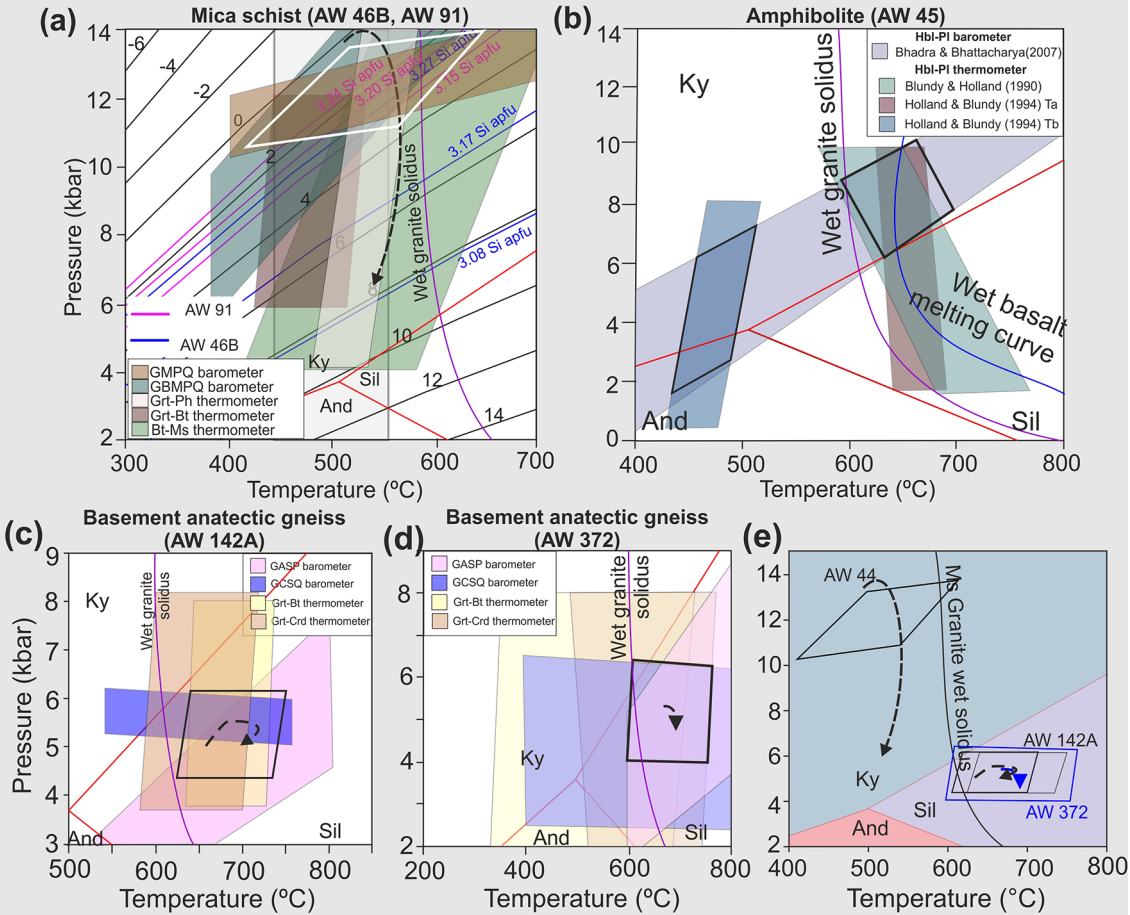
(a)
Mica schist (AW 46B, AW 91)
Pressure (kbar)
Temperature (ºC)
3.24 Si apfu
3.20 Si apfu
3.27 Si apfu
3.15 Si apfu
3.17 Si apfu
3.08 Si apfu
Wet granite solidus
AW 91
AW 46B
GMPQ barometer
GBMPQ barometer
Grt-Ph thermometer
Grt-Bt thermometer
Bt-Ms thermometer
Ky
Sil
And
(b)
Amphibolite (AW 45)
Hbl-Pl barometer
Bhadra & Bhattacharya(2007)
Hbl-Pl thermometer
Blundy & Holland (1990)
Holland & Blundy (1994) Ta
Holland & Blundy (1994) Tb
Wet granite solidus
Wet basalt melting curve
(c)
Basement anatectic gneiss (AW 142A)
GASP barometer
GCSQ barometer
Grt-Bt thermometer
Grt-Crd thermometer
(d)
Basement anatectic gneiss (AW 372)
(e)
AW 44
Ms Granite wet solidus
AW 142A
AW 372

Figure 8

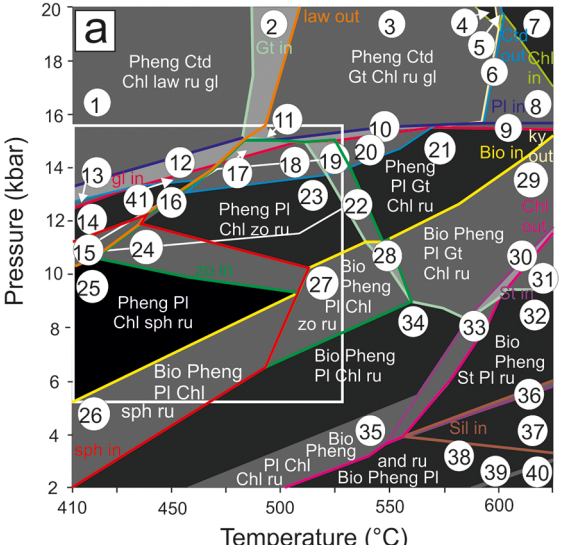

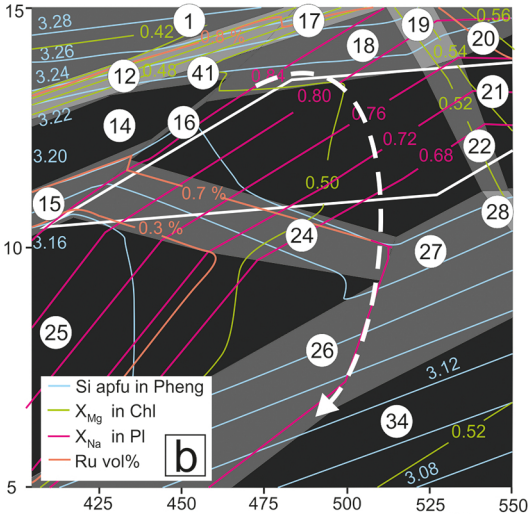

NCKFMASH-Ti system

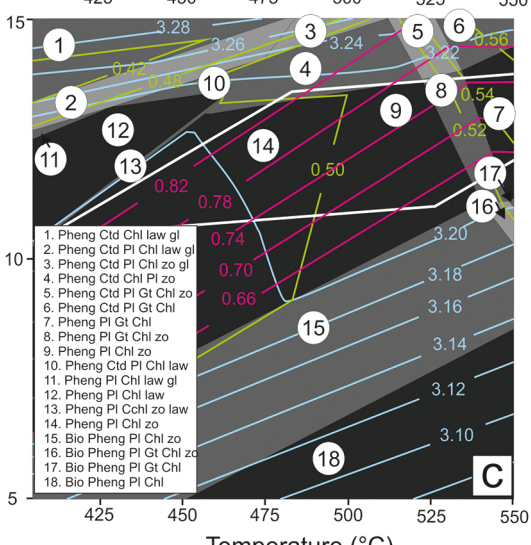

NCKFMASH system

Phase fields for NCKFMASH-Ti system (a, b)

1. Pheng Ctd Chl law ru gl
2. Pheng Ctd Gt Chl law ru gl
3. Pheng Ctd Gt Chl ru gl
4. Pheng Ctd Gt ru gl
5. Pheng Ctd Gt ky ru gl
6. Pheng Ctd Gt Chl ky ru gl
7. Pheng Gt ky ru gl
8. Pheng Gt Chl ky ru gl
9. Pheng Pl Gt Chl ky ru gl
10. Pheng Ctd Pl Gt Chl ru gl
11. Pheng Ctd Gt Chl zo ru gl
12. Pheng Ctd Pl Chl law ru gl
13. Pheng Pl Chl law ru gl
14. Pheng Pl Chl law ru
15. Pheng Pl Chl law sph ru
16. Pheng Pl Chl zo law ru
17. Pheng Ctd Pl Chl zo ru gl
18. Pheng Ctd Pl Chl zo ru
19. Pheng Ctd Pl Gt Chl zo ru
20. Pheng Ctd Pl Gt Chl ru
21. Pheng Pl Gt Chl ru
22. Pheng Pl Gt Chl zo ru
23. Pheng Pl Chl zo ru
24. Pheng Pl Chl zo sph ru
25. Pheng Pl Chl sph ru
26. Bio Pheng Pl Chl sph ru
27. Bio Pheng Pl Chl zo ru
28. Bio Pheng Pl Gt Chl zo ru
29. Bio Pheng Pl Gt Chl ru
30. Bio Pheng St Pl Gt Chl ru
31. Bio Pheng St Pl Gt ru
32. Bio Pheng St Pl ru
33. Bio Pheng St Pl Chl ru
34. Bio Pheng Pl Chl ru
35. Bio Pheng Pl Chl Chl ru
36. Bio Pheng St Pl sil ru
37. Bio Pheng Pl sil ru
38. Bio Pheng Pl and ru
39. Bio Pheng Pl San and ru
40. Bio Pl San and ru
41. Pheng Ctd Chl P law rul

Rock composition (wt%)	MnO	Na2O	CaO	K2O	FeO	MgO	Al2O3	SiO2	H2O	TiO2
	0.1	0.75	0.5	4.75	6.95	3.96	19.24	excess	excess	0.83

AW 44 (Mica schist)

Figure 9

AW 142A (Basement anatectic gneiss)

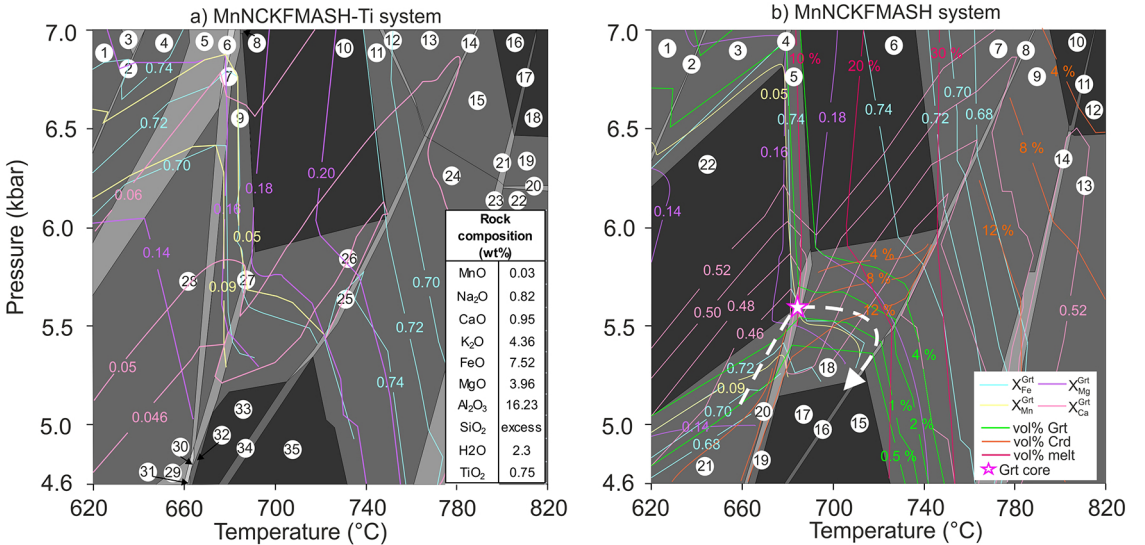

1. Bio St Pl Mica Gt Ilm H2O
2. Bio St Pl Mica Gt Sill Ilm H2O
3. Bio St Pl Mica Gt Ru Ilm H2O
4. Bio Pl Mica Gt Sill Ilm H2O
5. Bio Pl Mica Gt Sill Ilm H2O
6. Bio Pl Mica Gt Melt Sill Ru Ilm H2O
7. Bio Pl Gt Melt Sill Ru Ilm H2O
8. Bio Pl Gt Melt Sill Ru Ilm
9. Bio Pl Gt Melt Sill Ilm H2O
10. Bio Pl Gt Melt Sill Ilm
11. Bio Pl San Gt Melt Sill Iilm
12. Bio San Gt Melt Sill Ru Ilm
13. Bio Pl San Gt Melt Sill Ru
14. Crd Bio Pl San Gt Melt Sill Ru
15. Crd Bio Pl San Gt Melt Ru
16. Crd Bio San Melt Ru
17. Crd Opx Bio San Gt Melt Ru
18. Crd Opx San Gt Melt Ru
19. Crd Opx Pl San Gt Melt Ru
20. Crd Opx Pl San Gt Melt Ru Ilm
21. Crd Opx Bio Pl San Gt Melt Ru
22. Crd Opx Pl San Gt Melt Ilm
23. Crd Opx Bio Pl San Gt Melt Ilm
24. Crd Bio Pl San Gt Melt Ilm
25. Crd Bio Pl San Gt Melt Sill Ilm
26. Crd Bio Pl Gt Melt Sill Ilm
27. Crd Bio Pl Gt Melt Sill Ilm H2O
28. Bio Pl Gt Sill Ru Ilm H2O
29. Crd Bio Pl Gt Sill Ru Ilm H2O
30. Crd Bio Pl Gt Melt Sill Ru Ilm H2O
31. Crd Bio Pl Melt Sill Ru Ilm H2O
32. Crd Bio Pl Melt Sill Ilm H2O
33. Crd Bio Pl Melt Sill Ilm
34. Crd Bio Pl San Melt Sill Ilm
35. Crd Bio Pl San Melt Ilm

1. Bio St Pl Mica Gt H2O
2. Bio St Pl Mica Gt Sill H2O
3. Bio Pl Mica Gt Sill H2O
4. Bio Pl Mica Gt Melt Sill H2O
5. Bio Pl Gt Melt Sill H2O
6. Bio Pl Gt Melt Sill
7. Bio Pl San Gt Melt Sill
8. Crd Bio Pl San Gt Melt Sill
9. Crd Bio Pl San Gt Melt
10. Crd Bio San Gt Melt
11. Crd OpxBio San Melt
12.Crd Opx San Melt
13. Crd Opx Pl San Gt Melt
14. Crd Oopx Bio Pl San Gt Melt
15. Crd Bio Pl San Melt
16. Crd Bio Pl San Melt Sill
17. Crd Bio Pl Melt Sill
18. Crd Bio Pl Gt Melt Sill
19. Crd Bio Pl Melt Sill H2O
20. Crd Bio Pl Gt Melt Sill H2O
21. Crd Bio Pl Gt Sill H2O
22. Bio Pl Gt Sill H2O

Figure 10

AW 372 (Basement anatectic gneiss)

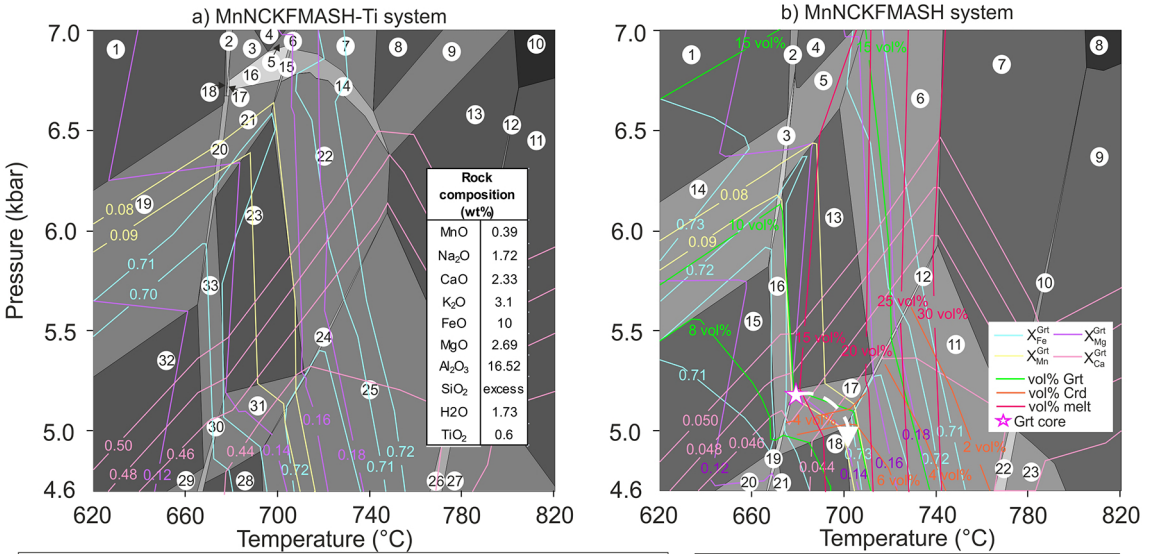

1. Bio Pl Mica Gt Ilm H2O
2. Bio Pl Mica Gt Melt Ru Ilm H2O
3. Bio Pl Mica Gt Melt Ru Ilm
4. Bio Pl Mica Gt Melt Ru
5. Bio Pl Mica Gt Melt Sill Ru
6. Bio Pl San Mica Gt Melt Sill Ru
7. Bio Pl San Gt Melt Sill
8. Bio Pl San Gt Melt Ru
9. Bio Pl San Gt Melt Ru Ilm
10. Pl San Gt Melt Ilm
11. Opx Pl San Gt Melt Ilm
12. Opx Bio Pl San Gt Melt Ilm
13. Bio Pl San Gt Melt Ilm
14. Bio Pl San Gt Melt Sill Ru Ilm
15. Bio Pl San Mica Gt Melt Sill Ru Ilm
16. Bio Pl Mica Gt Melt Sill Ru Ilm
17. Bio Pl Mica Gt Melt Sill Ru Ilm H2O
18. Bio Pl Mica Gt Melt Ilm H2O
19. Bio Pl Mica Gt Sill Ilm H2O
20. Bio Pl Mica Gt Melt Sill Ilm H2O
21. Bio Pl Mica Ggt Melt Sill Ilm
22. Bio Pl San Gt Melt Sill Ilm
23. Bio Pl Gt Melt Sill Ilm
24. Crd Bio Pl San Gt Melt Sill Ilm
25. Crd Bio Pl San Gt Melt Ilm
26. Crd Opx Bio Pl San Gt Melt Ilm
27. Crd Opx Pl San Gt Melt Ilm
28. Crd Bio Pl Gt Melt Ilm
29. Crd Bio Pl Gt Sill Ilm H2O
30. Crd Bio Pl Gt Melt Sill Ilm H2O.
31. Crd Bio Pl Gt Melt Sill Ilm
32. Bio Pl Gt Sill Ilm H2O
33. Bio Pl Gt Melt Sill Ilm H2O

1. Bio Pl Mica Gt H2O
2. Bio Pl Mica Gt Melt H2O
3. Bio Pl Mica Gt Melt Sill H2O
4. Bio Pl Mica Gt Melt
5. Bio Pl Mica Gt Met Sill
6. Bio Pl San Gt Melt Sill
7. Bio Pl San Gt Melt
8. Pl San Gt Melt
9. Opx Ppl San Gt Melt
10. Opx Bio Pl San Gt Melt
11. Crd Bio Pl San Gt Melt
12. Crd Bio Pl San Gt Melt Sill
13. Bio Pl Gt Melt Sill
14. Bio Pl Mica Gt Sill H2O
15. Bio Pl Gt Sill H2O
16. Bio Pl Gt Melt Sill H2O
17. Crd Bio Pl Gt Melt Sill
18. Crd Bio Pl Gt Melt
19. Crd Bio Pl Gt Melt Sill H2O
20. Crd Bio Pl Gt Sill H2O
21. Crd Bio Pl Gt Melt H2O
22. Crd Opx Bio Pl San Gt Melt
23. Crd Opx Pl San Gt Melt

Figure 11

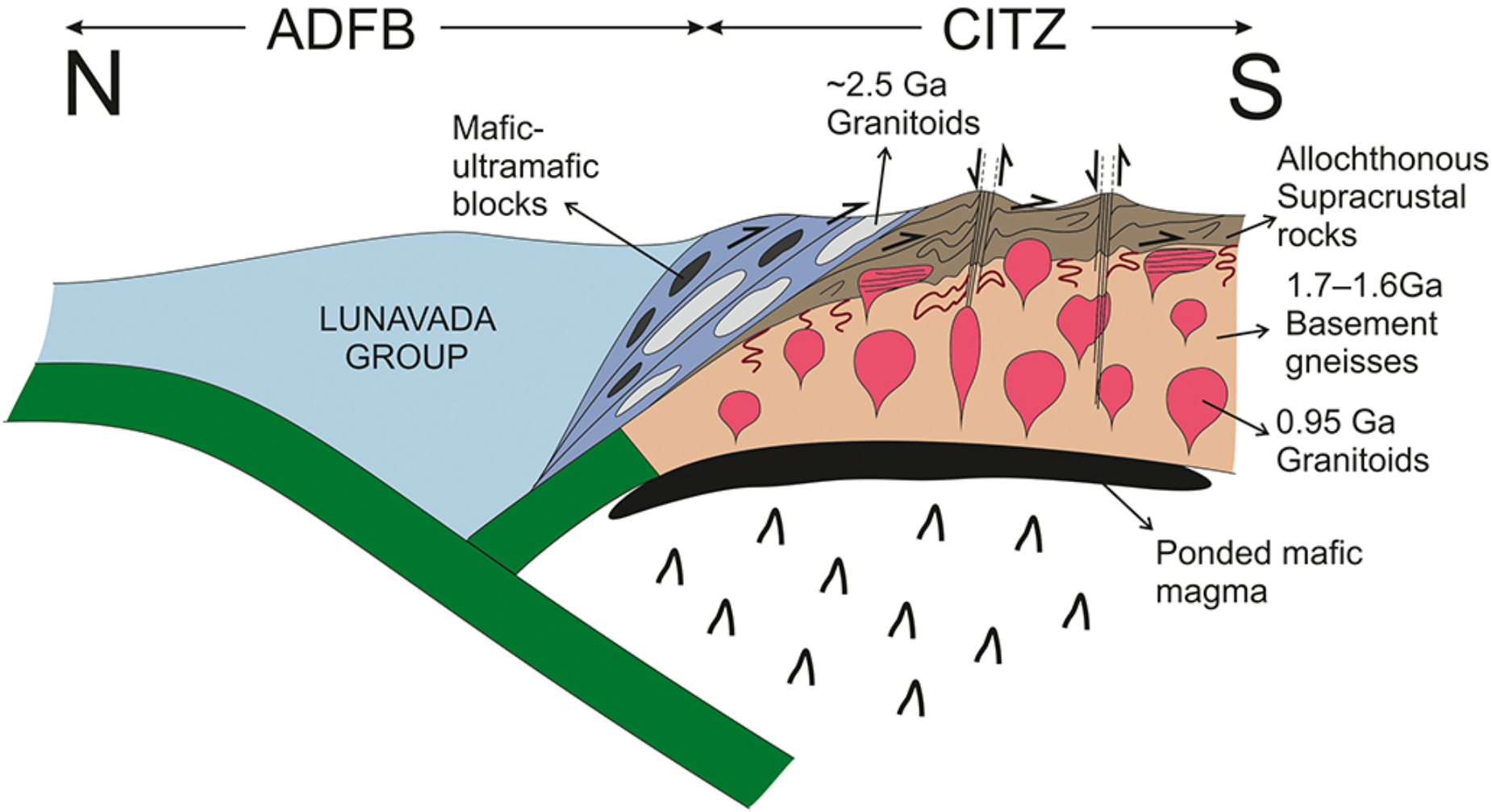
ADFB
CITZ
N
S
~2.5 Ga
Granitoids
Mafic-
ultramafic
blocks
Allochthonous
Supracrustal
rocks
1.7–1.6Ga
Basement
gneisses
LUNAVADA
GROUP
0.95 Ga
Granitoids
Ponded mafic
magma

Figure 12